Mineralium Deposita (2020) 55:107–130
https://doi.org/10.1007/s00126-019-00878-4

ARTICLE

Age, geological setting, and paragenesis of heavy rare earth element mineralization of the Tanami region, Western Australia

Teimoor Nazari-Dehkordi[1] · Carl Spandler[1] · Nicholas H. S. Oliver[1,2] · Robin Wilson[3]

Received: 29 August 2018 / Accepted: 22 March 2019 / Published online: 2 May 2019

Abstract

Metasedimentary rock-hosted heavy rare earth element (HREE) mineralization occurs as numerous orebodies distributed across a large district of the Tanami region of central Australia, close to a regional unconformity between Archean metasedimentary rocks of the Browns Range Metamorphics (BRM) and overlying Proterozoic Birrindudu Group sandstones. The orebodies consist predominantly of quartz, xenotime, and minor florencite and occur along steeply dipping structures within a stockwork of hydrothermal veins and breccias. Paragenetic stages of the mineralization include (1) a pre-ore stage of a greenschist-facies overprint of detrital minerals including quartz, alkali feldspar, plagioclase, and muscovite aligned in the premineralization foliation; (2) syn-ore quartz and white mica alteration associated with a multistage mineralization of the ore minerals, primarily in breccias and veins; and (3) a post-ore stage of veining and brecciation forming several generations of quartz, plus hematite, barite, anhydrite, and pyrite. In situ U–Pb dating of xenotime from several deposits/prospects yielded an age range for mineralization of 1.65 to 1.60 Ga; this timeframe lacks local magmatism or orogeny and is significantly younger than the ca. 1.72 Ga $^{40}Ar/^{39}Ar$ age of the pre-ore muscovite. Far-field stresses associated with the distal Isan and Liebig Orogenies are invoked as drivers of large-scale fluid flow and fault (re)activation in the region. We propose that ore formation was achieved via fluid leaching of REE from the BRM, followed by fluid mixing in fault zones, especially in the vicinity of the unconformity between the BRM and overlying Birrindudu Group sandstones. This mineralization style shares many features with unconformity-related U deposits, and there is significant potential for discovery of further REE orebodies of this style, especially in the vicinity of regional unconformities, in intercontinental sedimentary basins.

Keywords Rare earth elements · Xenotime · Unconformity · Isotopic dating · Tanami region

Introduction

Rapid development in high-technology applications such as permanent magnets and renewable energy technologies has promptly increased the demand for rare earth elements (REE). Currently, most of the world's REE supplies come from a single orebody, the Bayan Obo REE–Nb–Fe deposit, China; this restricted source represents a potential geopolitical instability in ongoing global REE supply. Furthermore, both heavy (H) and light (L) REE are sought-after commodities, yet most known REE resources across the world, including at Bayan Obo, are rich in LREE. These issues have led to much higher price for HREE relative to LREE. The HREE, particularly Dy, are anticipated to have the highest supply risk in the near future (e.g., Goodenough et al. 2018). Accordingly, there is a strong incentive for discovery and understanding of REE orebodies, particularly those rich in HREE.

Elevated concentrations of the REE have been documented from a variety of geological settings (e.g., magmatic, sedimentary, metamorphic). However, the production of REE has traditionally been dominated by deposits associated with peralkaline silicate magmas and carbonatite-associated

Editorial handling: D. Huston

Electronic supplementary material The online version of this article (https://doi.org/10.1007/s00126-019-00878-4) contains supplementary material, which is available to authorized users.

✉ Carl Spandler
carl.spandler@jcu.edu.au

[1] Department of Geoscience, Economic Geology Research Centre, James Cook University, Townsville, QLD 4811, Australia

[2] HCOV Global Consultants, PO Box 3533, Hermit Park, QLD 4812, Australia

[3] Northern Minerals, PO Box 669, West Perth, WA 6872, Australia

complexes (e.g., Chakhmouradian and Zaitsev 2012; Goodenough et al. 2018), or supergene enrichment environments. Although reported from across the globe, these unusual alkaline or peralkaline rocks are rather minor in the geological rock record, and so to address the current shortage in the REE production, a range of other geological environments where REE can be concentrated into exploitable orebodies are being examined. Newly discovered HREE mineralization in northwestern Australia (Fig. 1) defines a poorly understood vein and breccia ore style with ore metals contained predominantly in xenotime [$(Y,HREE)PO_4$] and minor florencite [$LREEAl_3(PO_4)_2(OH)_6$] (Cook et al. 2013; Nazari-Dehkordi et al. 2018), in an area known as the North Australian HREE + Y mineral field (herein abbreviated to NAHREY) as proposed by Nazari-Dehkordi et al. (2018). Hosted by the metasedimentary rocks, the mineralization in the NAHREY mineral field appears as numerous discrete orebodies in the Tanami region (see Fig. 2) and so far one orebody in the Halls Creek Orogen (John Galt prospect; see Fig. 1). Currently defined mineral resources for the Tanami region are ca. 9 Mt at 0.63% total rare earth oxides (TREO) (Northern Minerals 2018). Wolverine is the largest known single deposit, with a total mineral resource of 4.97 Mt at 0.86 wt% TREO. Compared with other REE deposits from across the globe, Wolverine is of relatively low tonnage and low grade (Fig. 3) but is remarkably rich in highly sought-after HREE (HREE = 89% by mass of TREO at Wolverine; see Table 1). The recognition and characterization of this style of mineralization has significant implications for further discovery of HREE, particularly in the North Australian Craton, with widespread Precambrian metasedimentary rocks of potentially suitable age and geochemistry.

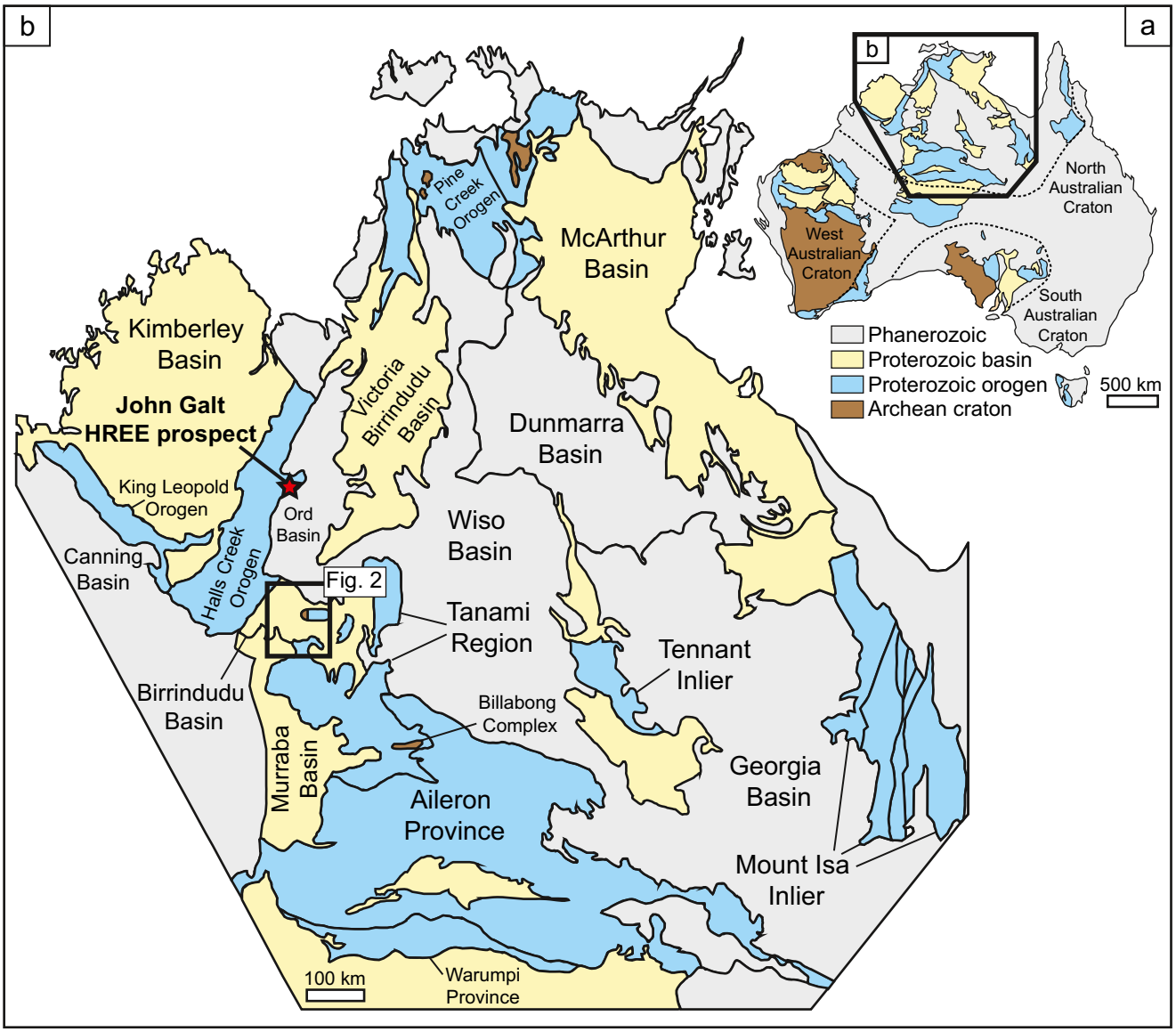

Fig. 1 **a** Simplified geological map of Australia showing the three major Australian Cratons. **b** Simplified geological map of the North Australian Craton

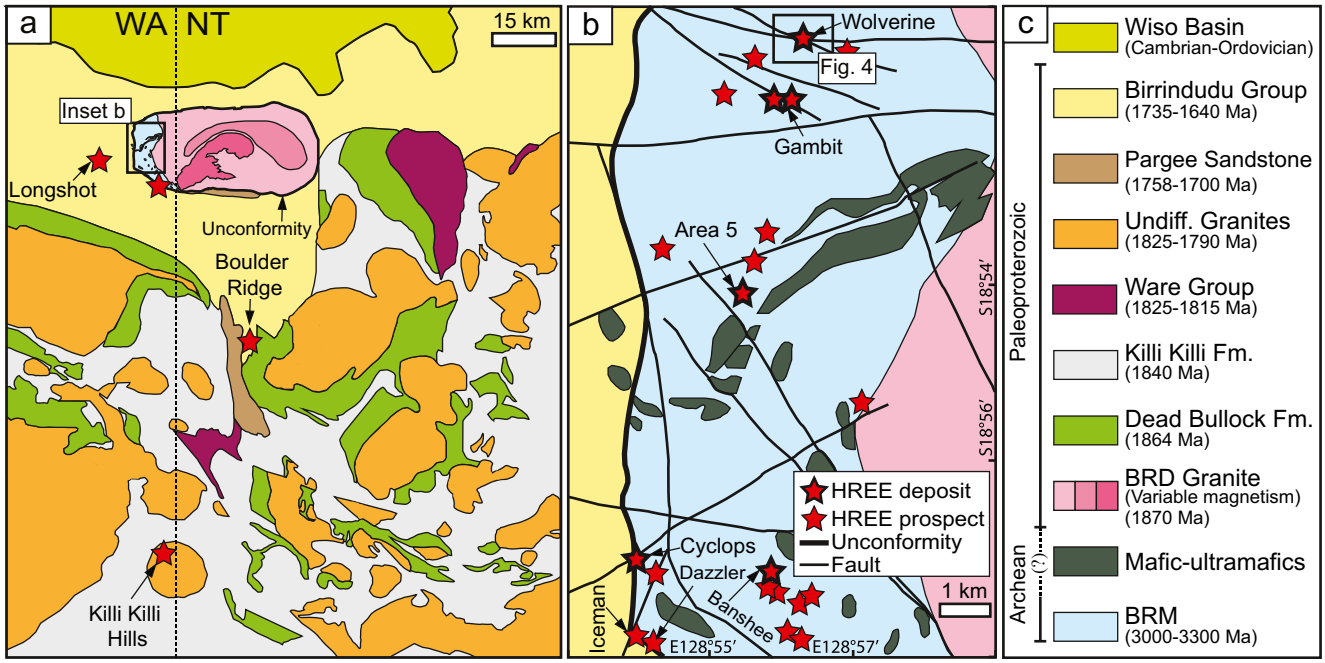

Fig. 2 **a** Simplified geological map of the Tanami region (modified after Bagas et al. 2008). **b** Geological map of the western margin of the Browns Range Dome (after Hendrickx et al. 2000) showing the location of the HREE deposits/prospects. **c** Major rock units in the Tanami region (after Crispe et al. 2007)

In such remote locations where geological relationships are only broadly known, knowledge of the temporal development of mineralization can greatly aid in the understanding of the geological history of the district and the processes responsible for ore deposit formation. Xenotime can form over a broad range of geological conditions and is a very useful U–Pb

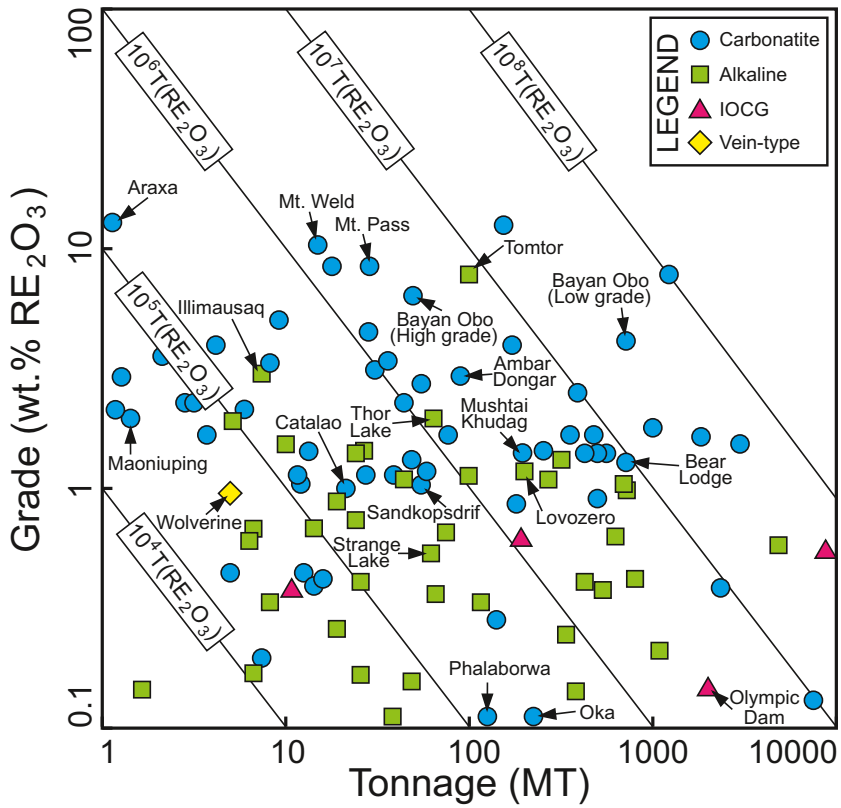

Fig. 3 Grade versus tonnage for REE deposits worldwide (modified after Weng et al. 2015). Well-known deposits are labeled. Note that Wolverine has a relatively low tonnage and grade but it is distinctly enriched in HREE

Table 1 Characteristics of the main HREE deposits/prospects in northern Australia

	Longitude	Latitude	Host	Proximity to unconformity	Resource (Mt)	TREO (wt%)	%HREE	Ore strike	Age (Ga)	Other
Deposit										
Wolverine	128.9403	− 18.8595	BRM	Distal	4.97	0.86	89	WNW	1.65–1.50	
Area 5	128.9249	− 18.9024	BRM	Distal	1.52	0.29	69	260–320°	1.60	Florencite-rich
Cyclops	128.903	− 18.9518	BRM	Proximal	0.33	0.27	70	WSW	1.63	
Banshee	128.9289	− 18.9552	BRM	Distal	1.66	0.21	87	90–110°	n.a.	U-rich
Gambit	128.9442	− 18.8681	BRM	Distal	0.11	1.13	96	85–115°	n.a.	
West Gambit	128.9355	− 18.8692	BRM	Distal	0.39	1.07	89	80–90°	n.a.	
Prospect										
Dazzler	128.9082	− 18.9741	BRM	Proximal	n.a.	n.a.	n.a.	WSW	1.65–1.62	
Iceman	128.9122	− 18.9775	BRM	Proximal	n.a.	n.a.	n.a.	WSW	1.65–1.62	
Longshot	128.8198	− 18.9424	BG	Distal	n.a.	n.a.	n.a.	NNW	1.64	
Boulder Ridge	129.2552	− 19.8283	BG	Distal	n.a.	n.a.	n.a.	NNW	1.62–1.55	
John Galt	128.2252	− 17.2962	RRB	Distal	n.a.	n.a.	94	NNW	1.62	
Area 5 North	128.9276	− 18.8978	BRM	Distal	n.a.	n.a.	n.a.	n.a.	n.a.	Florencite-rich
Banshee South	128.9292	− 18.9582	BRM	Distal	n.a.	n.a.	n.a.	NNW	n.a.	
Nightcrawler	128.9295	− 18.8926	BRM	Distal	n.a.	n.a.	n.a.	E–W	n.a.	
Mystique	128.9373	− 18.9648	BRM	Distal	n.a.	n.a.	n.a.	n.a.	n.a.	
Rogue	128.9618	− 19.0095	BRM	Proximal	n.a.	n.a.	n.a.	WNW	n.a.	
Havok	128.9288	− 18.8607	BRM	Distal	n.a.	n.a.	n.a.	n.a.	n.a.	
Polaris	128.923	− 18.8719	BRM	Distal	n.a.	n.a.	n.a.	n.a.	n.a.	
Rockslider	128.935	− 18.9708	BRM	Distal	n.a.	n.a.	n.a.	WNW	n.a.	
Sabretooth	128.9512	− 18.9201	BRM	Distal	n.a.	n.a.	n.a.	E–W	n.a.	
Sway	128.9415	− 18.964	BRM	Distal	n.a.	n.a.	n.a.	E-W	n.a	

Based on the lateral distance to the regional unconformity, the deposits/prospects are classified as "proximal" (within 50 m of the unconformity) and "distal." Coordinate system WGS84

BRM = Browns Range Metamorphics, *BG* = Birrindudu Group sandstones, *RRB* = Red Rock Basin, *n.a.* = not available

chronometer for dating geological processes ranging from diagenesis (e.g., Fletcher et al. 2004 and references therein), low-grade through high-grade metamorphism (e.g., Dawson et al. 2003; Sheppard et al. 2007), to hydrothermal mineralization (e.g., Aleinikoff et al. 2016; Rabiei et al. 2017). In this paper, we present U–Pb geochronology of ore-related xenotime together with paragenetic relationships from a number of vein- and breccia-hosted HREE deposits/prospects to understand the genesis and temporal evolution of the NAHREY mineral field. We show that HREE mineralization across the field developed within a relatively restricted time window and has a spatial relationship with subvertical faults and regional unconformities. Given the age relations and geological setting, we also compare this mineralization style to the unconformity-related uranium deposits of Northern Australia and Athabasca Basin, Canada.

Geological setting

The HREE deposits/prospects of the NAHREY mineral field occur within the Tanami region and the Halls Creek Orogen (Fig. 1). A summary of the characteristics and location of all the deposits and prospects is provided in Table 1 and Fig. 2. Here, we focus on the Tanami region where all but one deposit/prospect are located. Most of the deposits/prospects are named after fictional characters of the iconic "X-Men" comic book series of Marvel Comics. Wolverine, Area 5, Banshee, Cyclops, Gambit, and West Gambit are classified as deposits, as defined by Northern Minerals Ltd. (Northern Minerals 2018), and all are located within the Browns Range Dome (BRD) of the Tanami region, as described below. Numerous other prospects have been identified within the Tanami region; many of these have potential to be significant HREE resources, but are currently awaiting further exploration work. This study investigates three of the known deposits (Wolverine, Area 5, and Cyclops) as well as the Dazzler, Longshot, and Boulder Ridge prospects, although the Wolverine deposit is the main focus of the study.

Tanami region

The BRD is an east–west-trending ovoid-shaped structure measuring ca. 60 km × ca. 30 km, situated in the northwest of the

Tanami region (Fig. 2). It is cored by a 1- to 3-km-thick, largely granitic body, herein named the BRD granite (Hendrickx et al. 2000), of ca. 1.87 Ga age that also includes abundant detrital zircons of ages peaking at ca. 3.1 Ga and ca. 2.5 Ga (Page et al. 1995; Cross and Crispe 2007). Archean metasedimentary and minor mafic rocks of the Browns Range Metamorphics (BRM) occupy the western section of the dome (Nazari-Dehkordi et al. 2017) and are overlain by Paleoproterozoic sedimentary rocks of the Pargee Sandstone to the south, and the Birrindudu Group to the north, west, and south-west (Fig. 2). However, distinction between the Pargee Sandstone and Birrindudu Group is ambiguous, as they are of comparable lithology and have comparable depositional ages and detritus sources (Cross and Crispe 2007; Crispe et al. 2007).

The BRM crops out over an area of ca. 100 km^2 (Fig. 2) and consists mainly of a sequence of greenschist-facies (but locally up to amphibolite grade) arkosic metasandstones locally interbedded with medium- to coarse-grained conglomerates and semipelitic schists and less common calc-silicate rocks and banded iron formations. Limited field exposure and deformation have so far precluded detailed stratigraphic descriptions of the sequence. Nazari-Dehkordi et al. (2017) constrained the timing of deposition of the BRM to between ca. 3.0 Ga and ca. 2.5 Ga, based on the age of the detrital zircons in the BRM and the emplacement timing of the small (tens to hundreds of meters) crosscutting granitic, syenitic, and pegmatitic intrusions.

Unconformably overlying the BRM is a thick sequence of Paleoproterozoic sedimentary rocks with rare volcanic units (Fig. 2), which have been described in detail by Bagas et al. (2008) and Crispe et al. (2007). The oldest Paleoproterozoic unit of the Tanami region is the ca. 1.86 to ca. 1.84 Ga Tanami Group, which is unconformably overlain by the ca. 1.83 to ca. 1.81 Ga Ware Group, and then the Mount Charles Formation (ca. 1.80 Ga; Crispe et al. 2007). These units were deformed, domed, and then intruded by extensive ca. 1.83 to ca. 1.79 Ga granitoids which was also synchronous with gold mineralization of the region (Bagas et al. 2007). These rock sequences are in turn unconformably overlain by shallow-dipping sedimentary rocks of the Pargee Sandstone and Birrindudu Group, both of which comprise eroded detritus from 1.83 to 1.79 granitoids, and were deposited between ca. 1.78 to ca. 1.64 Ga (Crispe et al. 2007). The ca. 6-km-thick Birrindudu Group (Blake et al. 1975) consists of three conformable units including the basal Gardiner Sandstone, the fine-grained calcareous Talbot Well Formation, and Coomarie Sandstone.

The Gardiner Sandstone, occupying a vast area of the Tanami region (Fig. 2), was deposited within a shallow marine to intertidal environments on a stable continental margin (Clark and Blockley 1960). The Gardiner Sandstone is weakly metamorphosed and mildly deformed and unconformably rests on the underlying deeply weathered and metamorphosed rocks of the BRM, Tanami Group, Ware Group, and Pargee Sandstone (Crispe and Vandenberg 2005). It forms the outer margins of the BRD, with gentle (5° to 25°) westerly dips in the west in the vicinity of the HREE mineralization and easterly dips in the east of the dome. The depositional age of the Gardiner Sandstone, and generally the Birrindudu Group, is constrained by the youngest detrital zircon age of ca. 1.7 Ga (Crispe and Vandenberg 2005; Nazari-Dehkordi et al. 2017) and the ca. 1.64 Ga age of the xenotime overgrowing detrital zircons of the Gardiner Sandstone of the Birrindudu Group at the Killi Killi Hills (Vallini et al. 2007, see Fig. 2). In the study area, the Gardiner Sandstone directly lies on the Mesoarchean-derived BRM, leaving a sedimentation hiatus of ca. 800 m.y. (Nazari-Dehkordi et al. 2017).

Analytical methods

Sampling and petrography

During a program of fieldwork, ore samples were collected from surface outcrops and drill cores acquired by Northern Minerals Ltd. Although sampling focused in and around the Wolverine deposit, representative samples of most of the deposits/prospects were collected. The samples were lightly brushed and washed in an ultrasonic bath to remove any contamination from drilling mud or soil. Representative samples were then prepared as thin sections for petrographic studies using conventional optical microscopy and scanning electron microscopy.

Whole-rock geochemistry analyses

On the order of 12,000 diamond core and drill chip samples were analyses for REE and selected major and minor elements as part of mineral exploration and resource definition work by Northern Minerals Ltd. All analytical work was completed by Intertek-Genalysis Mineral Services. The samples were dried, crushed, split, and pulverized. To ensure complete dissolution of refractory minerals (e.g., xenotime), a 0.25-g aliquot of each sample was fused with 2 g of Na_2O_2 within a nickel crucible by heating to 700 °C for at least 30 min. Once cooled, the quenched glass was dissolved with 2 ml of HCl. The final solution, which contained no solids, indicating a complete dissolution was then diluted to 500 ml with deionized water. The final solution was then analyzed by inductively coupled plasma mass spectrometry (ICP-MS). This procedure follows that of Meisel et al. (2002), which was especially designed to ensure complete dissolution and recovery of refractory minerals. The assay data can be provided by the authors on request.

Orebody modeling

The Leapfrog Geo 3D modeling software was used to visualize the ore geometry and the grade distribution at Wolverine deposit.

Assay data from core samples of approx. 300 individual drill holes were imported and projected into the 3D model. The ore grade (wt% TREO) was modeled as four shells of > 0.25 (high grade), 0.25–0.15, 0.15–0.10, and < 0.10 (low grade). To avoid artificial oscillations, the reconstructed shape of each shell was considered the best-fit smooth pattern connecting the corresponding grades through the drill cores. The distribution of the ore grades was used to aid the structural interpretations.

Electron probe microanalysis

Backscattered electron (BSE) imaging and mineral identification and characterization of samples were undertaken using a JEOL-JXA8200 super probe, housed at the Advanced Analytical Centre (AAC), James Cook University (JCU). Quantitative major element analysis of pre- and syn-ore white mica was conducted by wavelength dispersive spectrometry (WDS) from carbon-coated polished thin sections using a 20-nA beam defocused to 5 μm and accelerating voltage of 15 kV. The elements measured were Na, Fe, Ca, Si, K, Al, Mn, Cl, Mg, Ti, and F. Natural and synthetic standards were used for calibration and the Armstrong-CITZAF (phi-rho-Z) matrix correction procedure was applied to all analyses. Further information on the analytical conditions are presented in the Electronic supplementary materials—Appendix 1.

In situ xenotime U–Pb isotope geochronology

In situ laser ablation (LA) ICP-MS U–Pb dating of xenotime was conducted at the AAC, JCU, using a GeoLas Pro 193-nm excimer laser and a Bruker (formally Varian) 820-MS ICP-MS. The ICP-MS was tuned using the NIST 610 silicate glass standard to ensure approximately equal sensitivity of U, Th, and Pb (e.g., see Pettke et al. 2012) to minimize isotope fractionation due to matrix effects. Laser fluence (energy density at the sample site) and pulse rate were set to optimal conditions of 6 J/cm^2 and 10 Hz, based on testing of laser parameters with the z6413 xenotime standard. Further details of the instrumental and analytical setup are available in Spandler et al. (2016). Analytes collected were ^{31}P, ^{89}Y, ^{204}Pb, ^{206}Pb, ^{207}Pb, ^{208}Pb, ^{232}Th, ^{235}U, and ^{238}U. The standards used for calibration include z6413 (primary) (^{206}Pb/^{238}U 993.8 ± 0.7 Ma; Stern and Rayner 2003), MG-1 (secondary), and BS-1 (secondary) xenotime (Fletcher et al. 2004). All analyses were undertaken using a 24-μm beam diameter, and data reduction was carried out using the GLITTER software (Van Achterbergh et al. 2001). All time-resolved single isotope signals from standards and samples were filtered for signal spikes or perturbations related to inclusions and fractures. Subsequently, the most stable and representative ratios were selected taking into account possible mixing of different age domains and zoning. Isoplot/Ex Version 4.15 (Ludwig 2009) was used to generate concordia plots and age calculations. Common Pb corrections were not applied given the very low levels of ^{204}Pb measured (Electronic supplementary materials—Appendix 2). The accuracy of the technique is demonstrated via analysis of secondary standards MG-1 and BS-1; these returned ^{206}Pb/^{238}U ages of 492 ± 3 Ma and 506 ± 5 Ma, respectively, which compare well with the published values of 490.0 ± 0.3 Ma for MG-1 and 508.9 ± 0.3 Ma for BS-1 (Fletcher et al. 2004).

^{40}Ar–^{39}Ar geochronology

Five samples of foliation-aligned pre-ore muscovite were selected from both well-mineralized and weakly mineralized samples of metasedimentary rocks of the Wolverine and Area 5 deposits. Further information on the source locations of these samples are provided in the Electronic supplementary materials—Appendix 3. The samples were crushed and sieved to 60 to 80 mesh (0.25 to 0.17 mm), and then white mica flakes were carefully handpicked to achieve about 95% purity. After cleaning in an ultrasonic ethanol bath, the grain separates underwent subsequent handpicking under a binocular microscope to achieve > 99% purity mineral separates. ^{40}Ar/^{39}Ar analyses were performed at the Argon Geochronology Laboratory of the University of Michigan using a continuous laser for step-heating and a VG 1200S noble gas mass spectrometer equipped with a Daly detector operated in analog mode using the methods outlined in Streepey et al. (2000) and Keane et al. (2006). Samples were wrapped in aluminum foil, loaded into an aluminum tube, then sealed into a quartz bottle and irradiated for 10.83 h at the McMaster nuclear reactor. Neutron flux gradients were monitored with the MMhb-1 standard using an age of 520.4 Ma (Samson and Alexander 1987). Following irradiation, 1 to 4 grains from each packet were loaded onto a copper disc that was placed into a gas extraction line. An Ar-ion laser, defocused to allow uniform heating, was used to heat the grains on the sample disc. Heating steps were performed for 30 to 60 s with a minimum power of 40 mW for the first step and a maximum power of 2000 mW for the last step. Isotopic ratios were measured on a MAP-215 mass spectrometer following the procedure described by Meert et al. (1994) and Busch et al. (1996). More details of the ^{40}Ar/^{39}Ar step-heating measurements are reported in the Electronic supplementary materials—Appendix 4.

Results

Geometry and geological setting of the Wolverine deposit

All of the examined HREE deposits/prospects have a spatial and an apparent kinematic relationship with faults and, in

many cases, lithological boundaries. The structural relationships with mineralization are best expressed by the Wolverine deposit, which lies along a WNW-striking fault at an intersection with a crosscutting N–E-trending fault (Fig. 4a). Long and cross sections (Fig. 4b, c) reveal Wolverine to be a typical vein-type orebody sitting within the steeply (~ 75° N) dipping WNW-striking fault. The orebody has a strike length of over 400 m and remains open to a depth of ca. 550 m and has no significant lateral or vertical ore metal zonation. The orebody appears to have developed either by dilation at this fault junction or by dilation due to bending along the WNW-striking fault. The displacement on the fault is as yet unknown, as there are few markers in the wall rocks. High-grade ore is defined by a stockwork of thick (up to 1 m) veins and breccia, surrounded by a halo of lower grade rock with thinner, broader spaced veins and less developed brecciation. A significant feature is the occurrence of discontinuities in the orebody accompanied by the development of low-grade ore into the host rock. These low-grade zones are inferred to represent minor post-ore remobilization, either as a product of supergene processes or as silica-rich fault zones infilled by HREE-poor veins late in the overall hydrothermal history.

Geological setting of the other HREE deposits/prospects

Despite their wide distribution, other BRM-hosted deposits/prospects predominantly occur near, or on, the unconformity with the overlying Gardiner Sandstone (e.g., Iceman, Dazzler, and Cyclops). These other deposits/prospects are dominated by hydrothermal mineralized veins and breccias that developed alongside major faults (Fig. 2); hence, they have many structural similarities with Wolverine. Mineralization tends to be developed along steeply dipping W- to SW-striking structures, or along the unconformity surface itself. The Area 5 deposit is distinguished by its high content of LREE compared to other deposits/prospects, as outlined below. Mineralization at Area 5 occurs at an intersection of subvertical fault zones with prominent W and NW strikes, alongside which the orebody appears as discontinuous pods.

Prospects hosted by the Gardiner Sandstone of the Birrindudu Group (Longshot, Boulder Ridge) also demonstrate close association with faults and regional unconformities. Longshot lies to the west of the BRD (Fig. 2a) at a location that is between 200 to 1200 m above the unconformity surface with the underlying BRM, as suggested by the available structural and geophysical data. Mineralization at Longshot occurs within irregular hydrothermal quartz-cemented veins and breccias developed along mostly NNW-striking steep fault structures that extend outwards and upwards from the BRD, thus showing structural and potentially genetic relationships with the BRM-hosted deposits/prospects. Similarly, xenotime–quartz vein mineralization at Boulder Ridge, located approx. 40 km south of the BRD, occurs near the unconformity with underlying metasedimentary rocks of the Tanami Group.

Bulk ore geochemistry

Ore minerals at all the deposits/prospects are limited to xenotime and florencite only (see below), yet there are notable variations in the geochemistry of the ore elements (REE + Y), as well as P and U between different deposits/prospects. In particular, we examine the compositional variants from the two largest and most diverse deposits Wolverine and Area 5. Bulk ore geochemistry of Wolverine is characterized by positive correlations between Ce (and LREE), Y (and HREE), U, and P (Fig. 5a–c), as may be expected for an ore mineral assemblage consisting of xenotime as the host of HREE, Y (and U), and florencite as the host of LREE. Ore from Wolverine extends to relatively higher U contents and shows a broad negative correlation with Ce (Fig. 5d), indicating

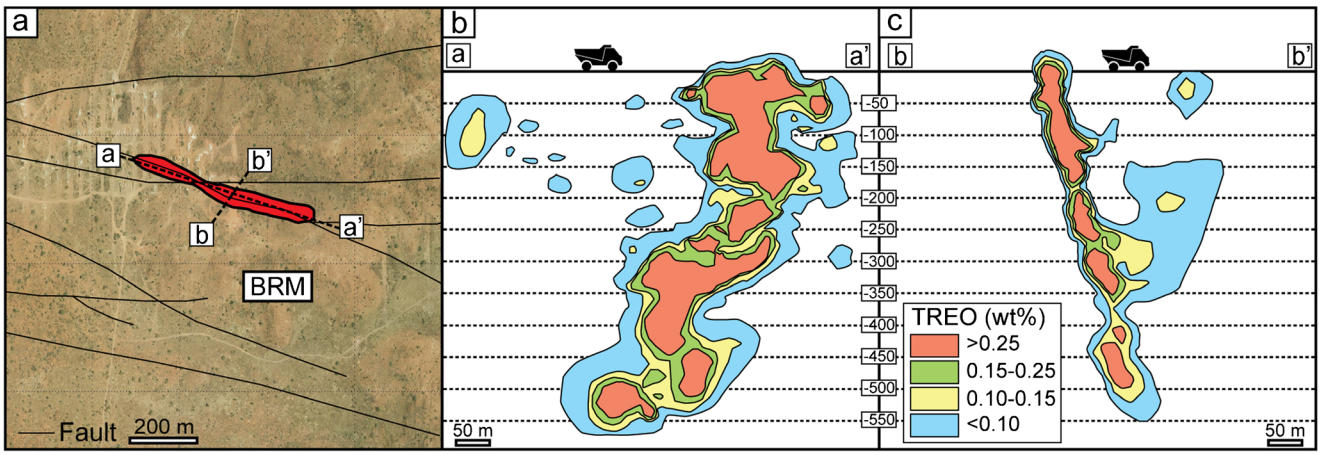

Fig. 4 Plan view (**a**) and long (**b**) and cross (**c**) sections of the Wolverine orebody represented by TREO grade shells. See Fig. 2b for location of the Wolverine deposit. Surface expression of the orebody is shown in red in **a**

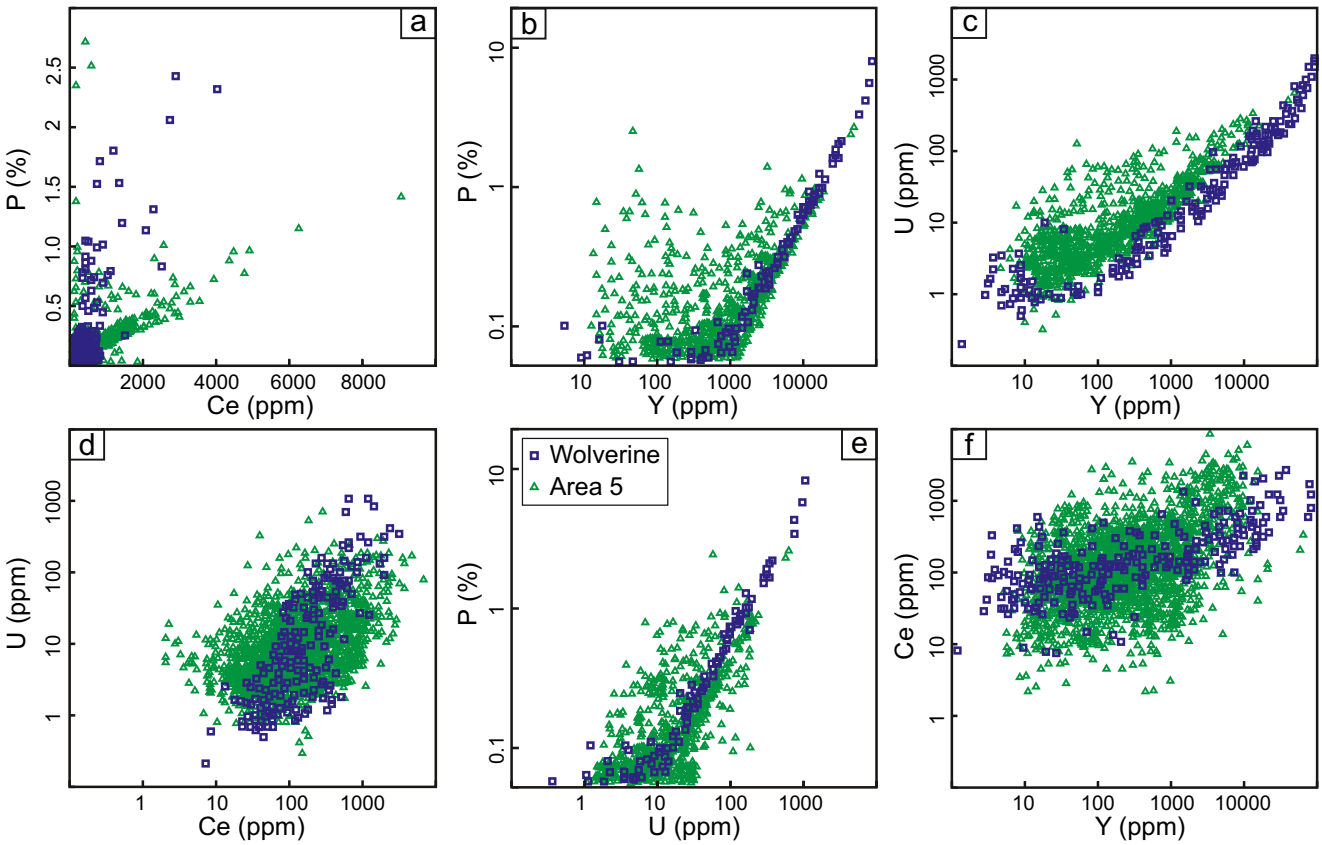

Fig. 5 **a**–**f** Scatterplots of P, Y, Ce, and U for whole-rock assay data from the Wolverine and Area 5 deposits

florencite is a relatively minor ore mineral and does not host most of the U. Strong positive relationship between U and Y (Fig. 5c) and U and P (Fig. 5e) at Wolverine, combined with the lack of other U-bearing minerals (e.g., uraninite), demonstrate that U is largely hosted in xenotime. Ore from Area 5 is comparatively poorer in P (Fig. 5a, b) and also shows an overall positive relationship between Ce, Y, U, and P (Fig. 5), although less well defined than at Wolverine. However, Area 5 ore extends to higher LREE contents than the other deposit (Fig. 5a, d, f), which is indicative of the relative dominance of LREE-rich florencite compared with HREE + Y-rich xenotime.

Compared to the orebodies, the nonmineralized BRM show relative enrichment in LREE (as is typical of clastic metasediments) and variable depletion in HREE (Nazari-Dehkordi et al. 2017, 2018). The distinctive HREE depletion was interpreted by Nazari-Dehkordi et al. (2018) to be due to HREE leaching by saline fluids.

We also use bulk-rock geochemistry data from the Wolverine deposit to examine alteration of major (i.e., none ore) elements within the host rock during the mineralization. Al–Si–K systematics (Fig. 6a) reveals a relatively broad compositional range for the unmineralized BRM, consistent with the occurrence of quartz, alkali feldspar (predominantly K-feldspar), and muscovite in various proportions, which is in agreement with petrographic observations (Nazari-Dehkordi et al. 2017), and likely represents protolith variations. Some highly aluminous samples represent kaolinite-rich alteration zones. Quite distinct from the nonmineralized rocks, almost all the bulk ore samples lie on, or close to, the muscovite (white mica) and quartz tie line, with much of the quartz as a key vein constituent with the ore minerals. This conversion of a range of original bulk compositions to a very specific muscovite–quartz composition is a typical indicator of large metasomatic fluid fluxes (Korzhinskii 1970), suggestive of association of the mineralization with a muscovite alteration. Ore formation is also associated with some Fe enrichment in the form of hematite (Fig. 6b) as found in some breccias and veins (see below). Nevertheless, overall, most ore samples do not have elevated Fe contents compared to the host BRM samples.

Ore mineral assemblage and paragenesis

A mineral paragenetic sequence was established on the basis of field observations and microscope petrographic studies. Although this paragenetic sequence is based mainly on the samples collected from Wolverine, available field, petrographic, geochemical, and isotopic data from across the NAHREY mineral field indicate remarkable consistency among the mineralization occurrences. The minerals associated with the

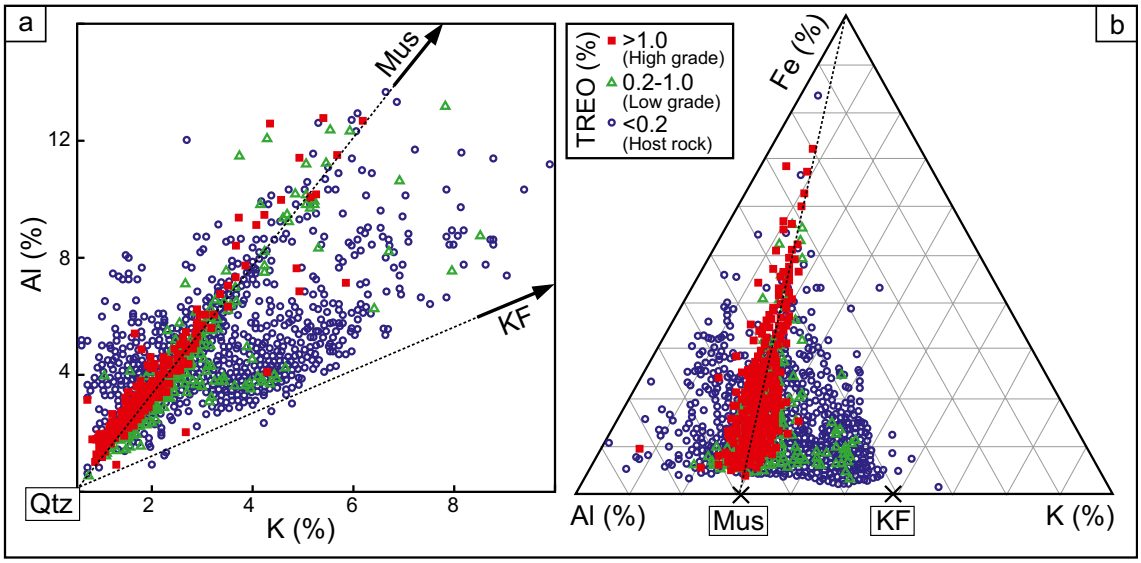

Fig. 6 **a** Whole-rock Al versus K and **b** Al–Fe–K ternary plot for the core samples (n = ca. 8300) from the Wolverine deposit. Compositions and tie lines between quartz (Qtz) and K-feldspar (KF) and quartz and muscovite–illite (Mus) are shown

orebody and the host metasedimentary rocks can be divided into three general categories: (1) detrital and metamorphic assemblages, which reflect mainly a greenschist-facies overprint on the predominantly meta-arkosic host rocks; (2) hydrothermal minerals related to the mineralization event(s); and (3) hydrothermal minerals that formed after the mineralization event(s) (Fig. 7).

Stage 1: premineralization alteration stage

The BRM consists of detrital phases including quartz and feldspar of variable morphology and size, and also detrital zircon. Detrital REE minerals are extremely scarce, although Nazari-Dehkordi et al. (2018) identified rare fine-grained (up to 5 μm) pitted and corroded REE phosphates (largely xenotime) of potentially detrital origin. However, subsequent metamorphic and hydrothermal overprints led to a nearly complete obliteration of the original grain textures and morphology (Nazari-Dehkordi et al. 2017). The first recognizable postsedimentation mineral/structural paragenesis in the BRM is a locally well-developed schistose foliation associated with the recrystallization of detrital quartz (Q1) into polycrystalline quartz patches (Q2) that have undulose extinction and tangential, concavo-convex, or sutured contacts between grains (Fig. 8a). These features are interpreted to be the result of deformation and greenschist-grade metamorphism related to the regional Tanami Event at ca. 1.83 Ga (Crispe et al. 2007).

The premineralization alteration stage also includes a sericite + muscovite (M1) alteration assemblage that replaced detrital alkali feldspar of the BRM (Fig. 8b). The white mica alteration manifests as platy coarse muscovite grains of up to 0.5 mm in length, aligned in the metamorphic foliation (Fig. 8b). This foliation-parallel assemblage occurs most prominently with mineralization but is traceable for several meters away from the orebodies. Additionally, hematite (H1) may occur as interlayers with sericite and larger muscovite grains (Fig. 8c) but is absent where overprinted by later alteration stages.

Stage 2: syn-mineralization alteration, veining and breccia

Syn-mineralization alteration consists dominantly of fine-grained quartz and muscovite–sericite–illite (white mica, M2) that also contains minor hematite (H2) developed mainly in the fault zones. The quartz appears as cavity- and fracture-filled quartz (Q3a), which typically displays radial extinction, cemented by finer grained quartz (Q3b) (Fig. 8d), and also as quartz replacing preexisting detrital quartz (Q2) (Fig. 8e). This fine-grained association is more intense adjacent to the HREE mineralization and related faults and is characterized in part by overprinting and replacement of the earlier-formed, foliation-parallel assemblages described above (Fig. 8b).

The syn-ore alteration event was succeeded by the earliest phase of the ore mineralization, herein called "breccia-hosted" mineralization. The breccia system is characterized by a set of chaotic and mosaic breccias occurring along steeply dipping major faults of usually a few meters width. The chaotic breccias tend to occupy a narrow (~ 1 m) core of the mineralized zone and are composed primarily of small rounded to subrounded clasts of the metasedimentary rocks of variable size (rarely > 3 cm), with no traces of earlier mineralization. The breccia matrix is largely composed of ore minerals and associated syn-ore quartz–white mica alterations. Chaotic breccias are enveloped by mosaic breccias, which consist mainly of medium to large (2 mm to > 20 cm) clasts of metasedimentary rocks that display a fitted-fabric texture.

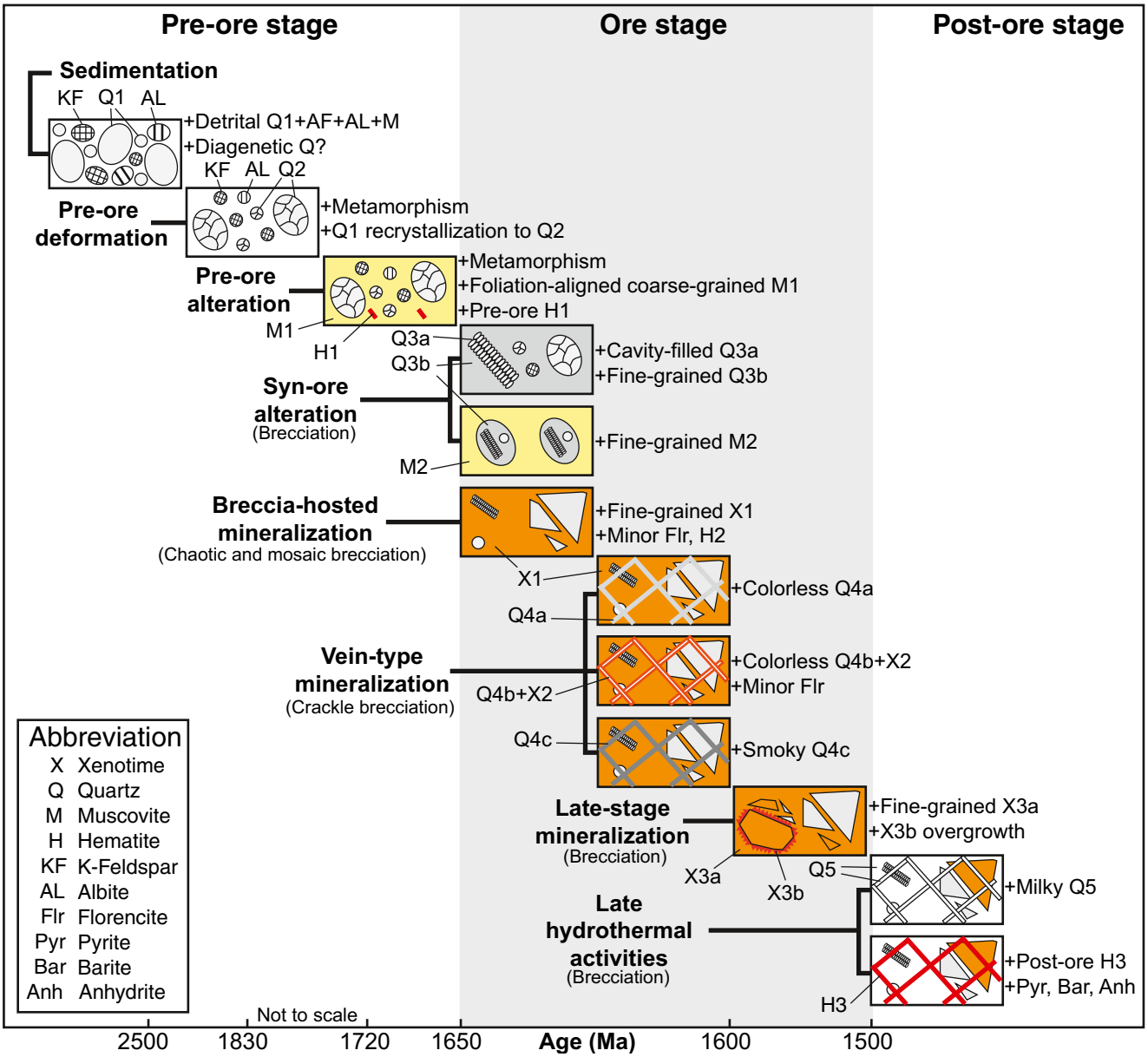

Fig. 7 Three-stage mineral paragenesis associated the HREE mineralization and the host metasedimentary rocks. See text for details

The mosaic breccias tend to occupy wider intervals (up to 4 m in width) of the mineralization zones, and host ore of variable grade, depending on the relative volume of the breccia matrix.

The breccia-hosted mineralization (Fig. 9a–e) is dominated by xenotime (X1) and minor florencite, which occur in the breccia matrix, as well as in fractures, cavities, and also within quartz–white mica alteration assemblages. Morphologically, X1 appears as clusters or as individual crystals (Fig. 10a) of dominantly anhedral grains that range in size from a few micrometers to over 200 μm. X1 also appears as pyramid-shaped overgrowths on detrital zircon (Fig. 10b). Xenotime (X1), particularly as coarser grains, is partially replaced by late florencite (Fig. 10c).

Stage 3: vein-type mineralization

The breccia-hosted mineralization and adjacent hosting rock are crosscut by hydrothermal veins (Fig. 9a–f), which in the most intense cases have formed crackle breccias in which the angular clasts of the metasedimentary rocks (themselves commonly already brecciated) are arranged in a jigsaw puzzle pattern with no major displacement. The hydrothermal veins vary from a few millimeters up to 20 cm in width and are composed of quartz (Q4) and xenotime (X2). Q4 includes multiple quartz types. Q4a is colorless and transparent quartz that predates xenotime (X2) (Fig. 11a), and likely marks the onset of the hydrothermal event associated with the "vein-

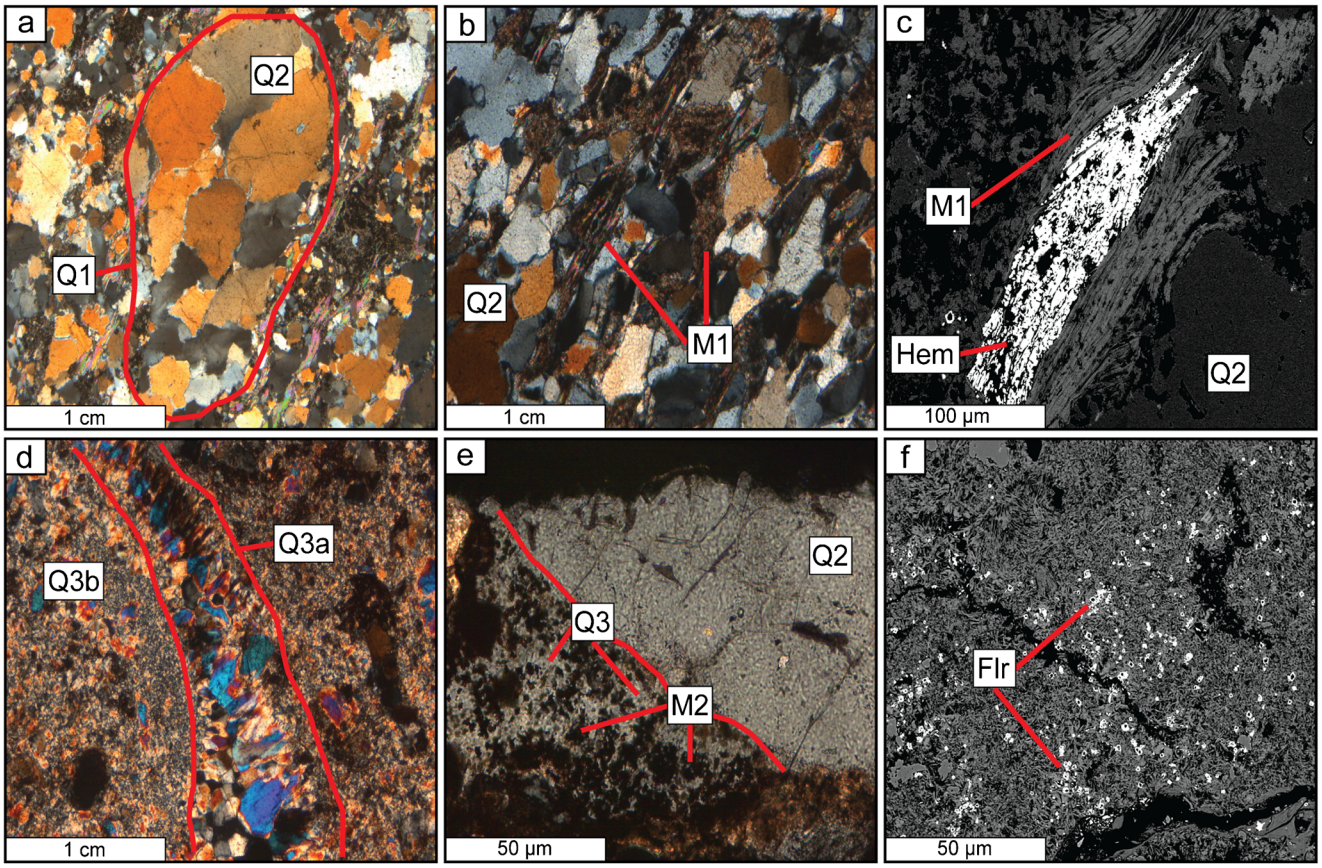

Fig. 8 Backscattered electron and cross-polarized transmitted-light microscopic images of samples of the BRM. **a** A primarily large detrital quartz (Q1) recrystallized into a polycrystalline quartz (Q2). **b** Course-grained muscovite aligned in the pre-ore foliation. **c** Interlayer of hematite and pre-ore course-grained muscovite. **d** Syn-ore quartz alteration appearing as cavity-filled (Q3a) and fine-grained (Q3b) in breccia. **e** Regrowth of a detrital quartz during quartz–white mica alteration. **f** Tiny authigenic florencite enclosed in clay. Q = quartz; M = muscovite; H = hematite; Flr = florencite

type" mineralization stage. X2 + Q4b veins overprint Q4a (Fig. 11a) and consist primarily of colorless quartz veins of usually ~ 1 cm in width, which are in turn cut by smoky Q4c veins that have a vuggy texture (Fig. 11b). In places, the primary X2 veins were reopened (Fig. 11c) or broken and offset (Fig. 11d) due to repeated fracturing and minor fault displacement of the host rocks.

Xenotime (X2) occurs as blade- or pyramid-shaped grains ranging in size from 50 to 1000 μm (Fig. 10d). X2 is usually fractured and pitted and displays subtle zoning in BSE images (Fig. 10e). Euhedral equant florencite grains (~ 1 to ~ 30 μm) occur within Q4 (Fig. 10f) or X2 (Fig. 10g) and are interpreted to be co-genetic to Q4 + X2 veins. Typically, large florencite grains demonstrate a subtle oscillatory zoning in BSE, in which the rim appears to be brighter than the core zone (Fig. 10f).

Stage 4: late-stage mineralization

The youngest xenotime mineralization event is represented by fine-grained euhedral xenotime (X3a) that dominantly occurs in breccias (Fig. 9g) containing mineralized and nonmineralized clasts (Fig. 10h) and pyramid-shaped xenotime overgrowths (X3b) on the preexisting xenotime (Fig. 10i). These are termed "late-stage" mineralization. X3 grains rarely exceed 30 μm in size and show no evidence for co-genetic florencite or quartz, although they are occasionally replaced by secondary florencite.

Stage 5: late hydrothermal phases

Post-dating the breccia-hosted and vein-type mineralization and their associated alteration are veins containing quartz (Q5), barite, anhydrite, pyrite, and hematite (H3). These veins (up to 10 cm in width) display vuggy and drusy textures and are distinguished by a characteristic milky color. They are composed primarily of several generations of large (1–5 cm in size) intergrown quartz (Fig. 11e). Occasionally, Q5 veins manifest as breccias (Fig. 11f) alongside previously mineralized major faults and fractures that may therefore contain mineralized clasts.

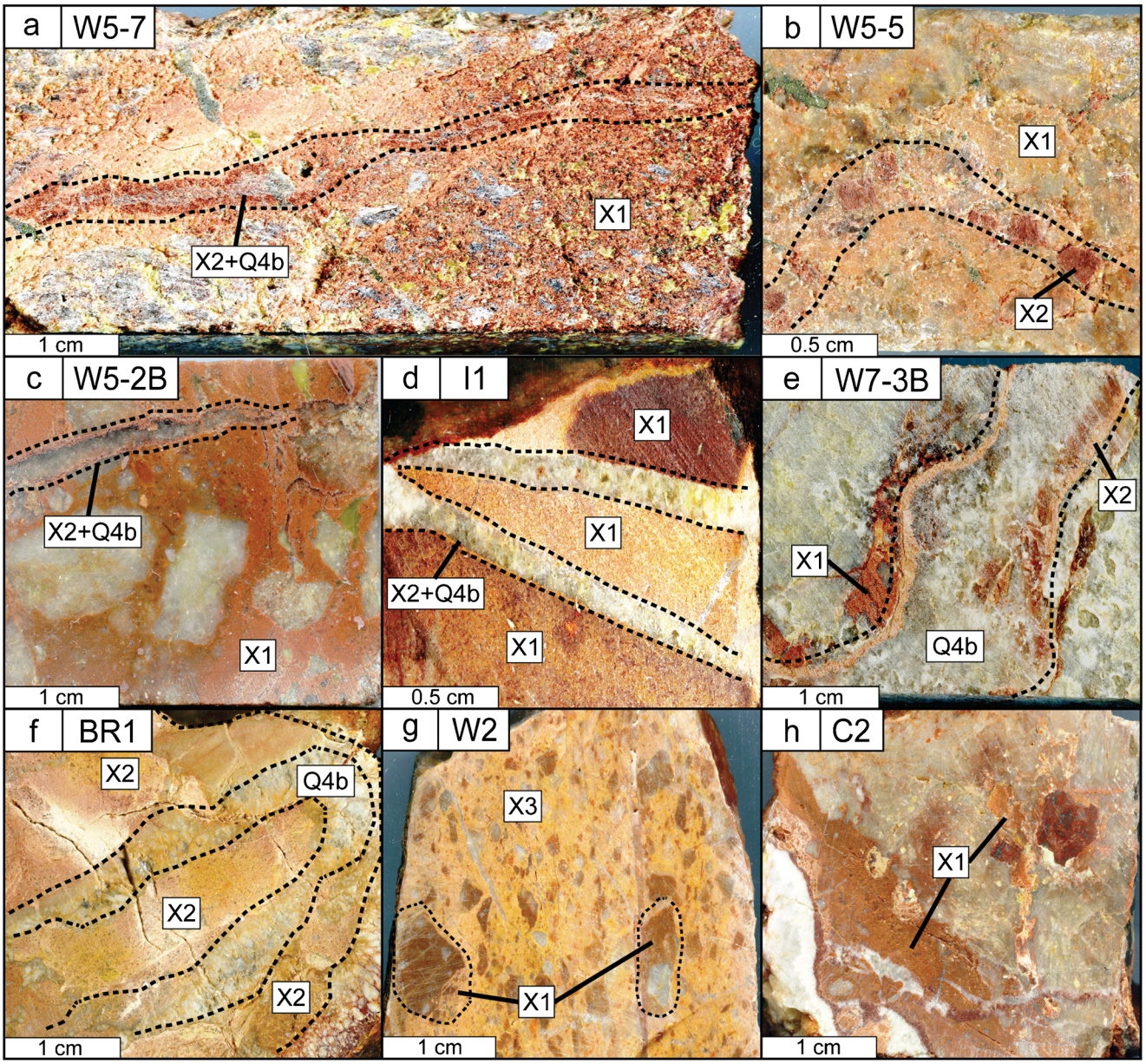

Fig. 9 Hand specimen photos of ore-related xenotime (X) and quartz (Q) from various HREE deposits/prospects: **a** sample W5-7; **b** sample W5-5; **c** sample W5-2B; **d** sample I1; **e** sample W7-3B; **f** sample BR1; **g** sample W2; **h** sample C2. Deposit abbreviation: W = Wolverine; I = Iceman; BR = Boulder Ridge; C = Cyclops

The final hydrothermal event of the paragenetic sequence is the partial replacement of pre- and syn-ore white mica by clays and clusters of tiny (< 5 μm) authigenic florencite grains that tend to have cubic forms with a skeletal texture in which only a narrow rim of the original grain remains (Figs. 8f and 10f).

White mica composition

A complete list of major element analyses of the pre- (M1) and syn-ore (M2) white mica is presented in the Electronic supplementary materials—Appendix 5. Both mica types have relatively low FeO, MnO, and TiO_2 contents and conform well to the muscovite [$KAl_2(Si_3Al)O_{10}(OH,F)_2$] to alumino-celadonite [$K(Mg,Fe^{2+})(Al)[Si_4O_{10}](OH)_2$] solid solution system (Rieder et al. 1999) and, hence, have phengitic compositions (Fig. 12a, b). The pre-ore mica has relatively low Si (Si a.p.f.u = 3.1 to 3.3) and K + Na a.p.f.u. close to 1, as is typical for natural muscovite. The syn-ore white mica extends to more phengitic compositions with higher Si contents (3.3 to 3.5 a.p.f.u.) and lower Al (2.2 to 2.5 a.p.f.u.) (Fig. 12a) and is K deficient, with K + Na a.p.f.u. between 0.75 and 0.88 (Fig. 12b). This interlayer deficiency is typical of illite series micas (Rieder et al. 1999) and may be due to pyrophyllite-type exchange of Si + vacancy = Al^{iv} + (K + Na) (Rosenberg

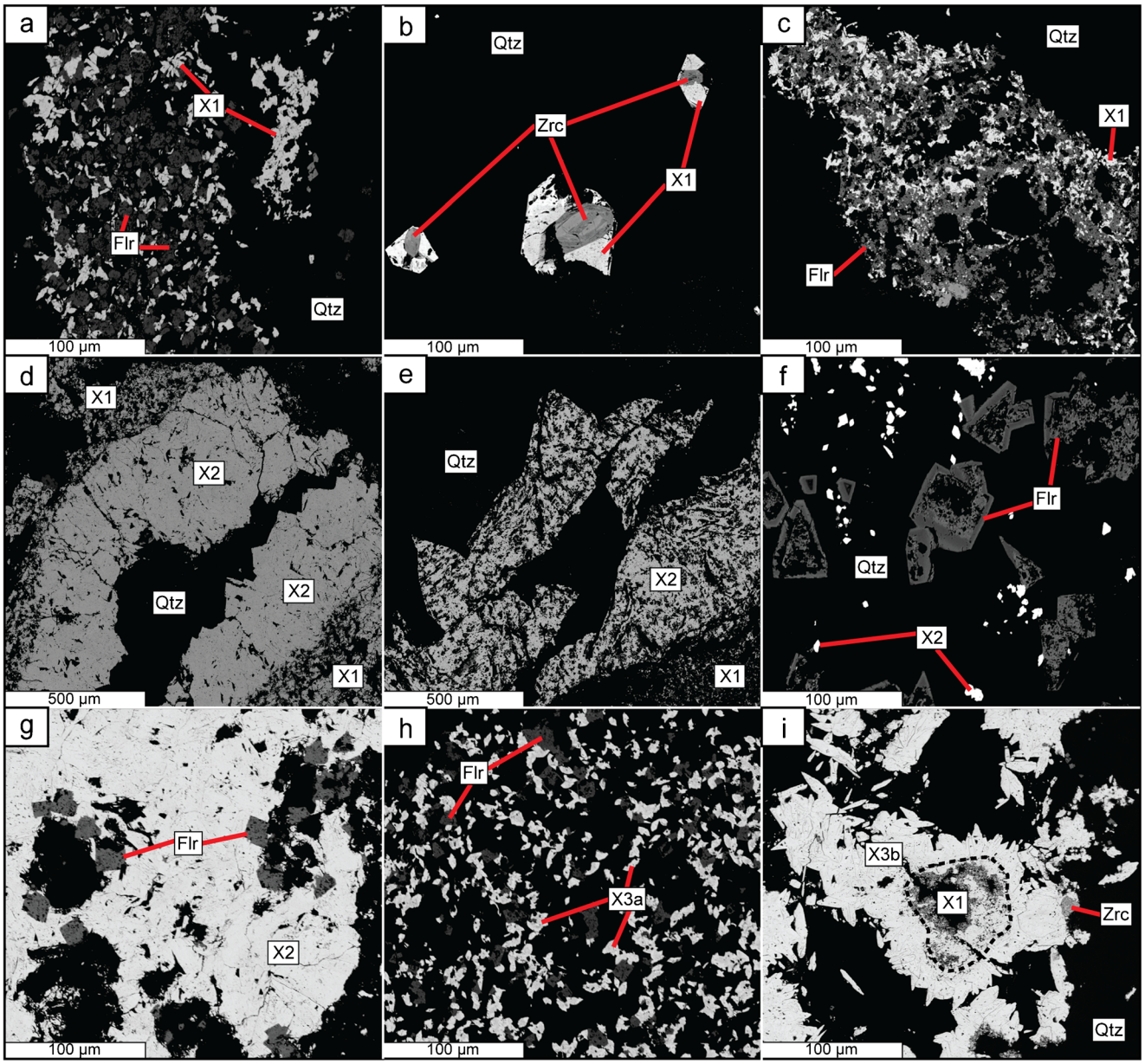

Fig. 10 Backscattered electron microscopic images of ore minerals from Wolverine deposit. **a** Euhedral to anhedral fine-grained breccia-hosted xenotime and associated florencite. **b** Xenotime overgrowing detrital zircons. **c** Breccia-hosted xenotime almost entirely replaced by florencite. **d** Course-grained vein-type xenotime crosscutting breccia-hosted xenotime. **e** Vein-type pyramid-shaped xenotime ore. **f** Florencite and xenotime distributed within a mineralized hydrothermal quartz vein. **g** Co-genetic xenotime and florencite. **h** Late fine-grained xenotime in the matrix of a breccia containing mineralized clasts. **i** Late pyramid-shaped xenotime overgrowing earlier fine-grained xenotime. Flr = florencite; Qtz = quartz; X = xenotime; Zrc = zircon

2002). Most notably, the syn-ore mica is significantly richer in F (up to 0.5 wt%) and Cl (up to 0.09 wt%) than the pre-ore muscovite (F = < 0.06 wt%; Cl = < 0.02 wt%) (Fig. 12c).

Geochronology

^{40}Ar–^{39}Ar geochronology of white mica

$^{40}Ar/^{39}Ar$ dating results of four premineralization white mica (M1) samples from Wolverine and one sample from Area 5 are presented in Table 2. Note, syn-ore (M2) white mica was too fine-grained to date with our methods. The quoted uncertainties in the ages incorporate uncertainties in the peak signals, system blanks, spectrometer mass discrimination, reactor corrections, and *J* values. Superficial ^{40}Ar loss observed in the samples had no major impact on the validity of the ages and Ar release spectra are relatively flat in all samples. The sample from Area 5 yielded a $^{40}Ar/^{39}Ar$ total gas age of 1727 ± 9 Ma, which is in the range of the ages of three samples from Wolverine (1712 ± 8, 1714 ± 9, 1719 ± 9 Ma). The final

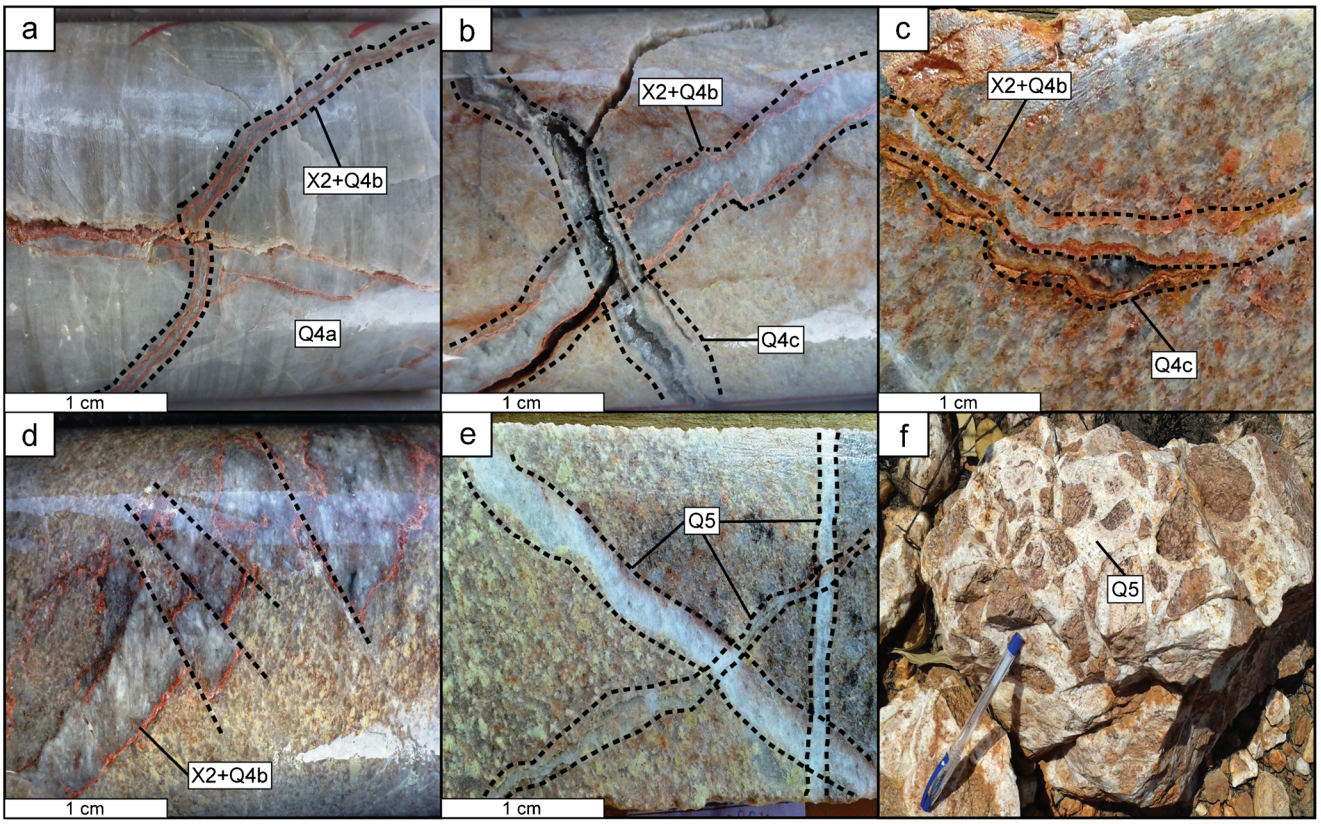

Fig. 11 Hydrothermal veins associated with the HREE mineralization. **a** Quartz–xenotime vein crosscutting a preexisting quartz vein. **b** Quartz–xenotime vein being cut by a smoky quartz vein. **c** Smoky quartz vein cutting a quartz–xenotime vein. **d** Minor fault dislocations of a quartz–xenotime vein. **e** Multiple generations of late milky quartz veins. **f** Late breccia containing milky quartz in the matrix. Q = quartz; X = xenotime

Wolverine sample returned a slightly older age of 1746 ± 9 Ma.

Uranium–Pb geochronology of xenotime

Fourteen samples from seven deposits/prospects were selected for U–Pb dating, including eight samples from Wolverine and one sample from each other deposit/prospect (Area 5, Cyclops, Dazzler, Longshot, Iceman, and Boulder Ridge), with relevant hand specimen images shown in Fig. 9. Uranium–Pb concordia diagrams, calculated ages, and isotope data for the samples are provided in Fig. 13 and Electronic supplementary materials—Appendix 2. Sample location information is provided in the Electronic supplementary materials—Appendix 3.

A total of 230 analyses were conducted on xenotime from breccia-hosted, vein-type, and late overgrowth xenotime grains (Fig. 13). Grains that were free of inclusion or fractures

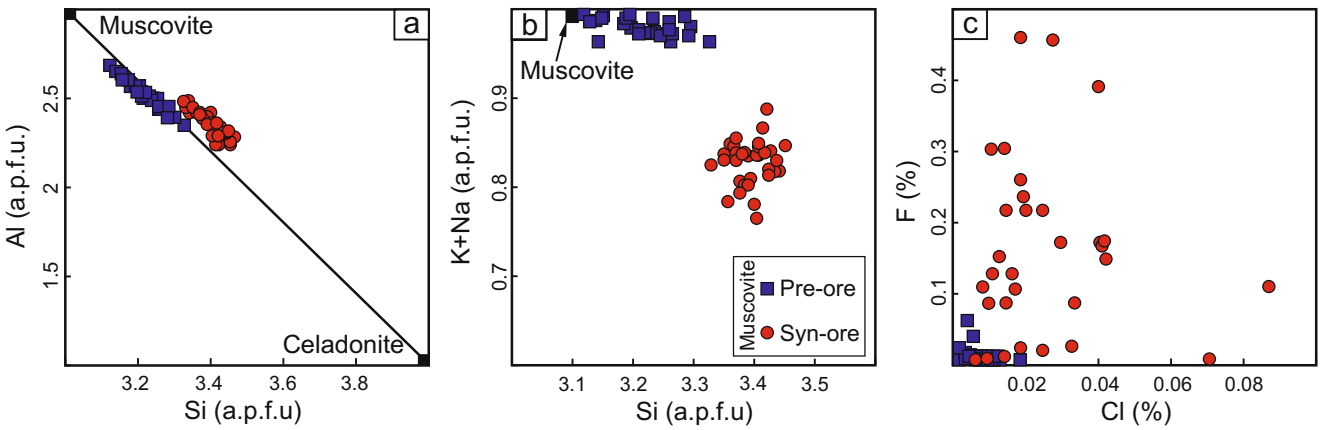

Fig. 12 Chemical composition of the pre- and syn-ore muscovite. **a** Aluminum (atoms-per-formula-unit; a.p.f.u.) versus Si (a.p.f.u.). **b** Si (a.p.f.u.) versus K + Na (a.p.f.u.). **c** F (wt%) versus Cl (wt%). Note: syn-ore muscovite is relatively enriched in F and Cl

Table 2 Ar-Ar data for pre-ore muscovite from the Wolverine and Area 5 deposits

	Sample No.	Deposit	Drill core	Depth (m)	Easting	Northing	Total gas age
1	A2-22	Area 5	BRAD0002	159.1	492,231.3	7,909,977	1727 ± 9
2	W5-4	Wolverine	BRWT0332W5	503.2	493,508.1	7,915,069	1746 ± 9
3	W5-6	Wolverine	BRWT0332W5	505.2	493,508.1	7,915,069	1714 ± 9
4	W5-8	Wolverine	BRWT0332W5	510.6	493,508.1	7,915,069	1712 ± 8
5	W324-7	Wolverine	BRWT0324	441.6	493,541.1	7,914,983	1719 ± 9

were targeted for analysis. The fine grain size of the breccia-hosted and late overgrowth xenotime dictated that only a single analyses could be made from each grain, whereas the course grain size of the vein xenotime allowed multiple analyses to be performed on a single grain.

Despite large variation in morphology, size, and age, BSE imaging only revealed rare faint domains (up to 5 μm) of zoning in xenotime, suggesting that most grains are largely homogeneous in composition. Xenotime analyses of differing generations from each deposit/prospect

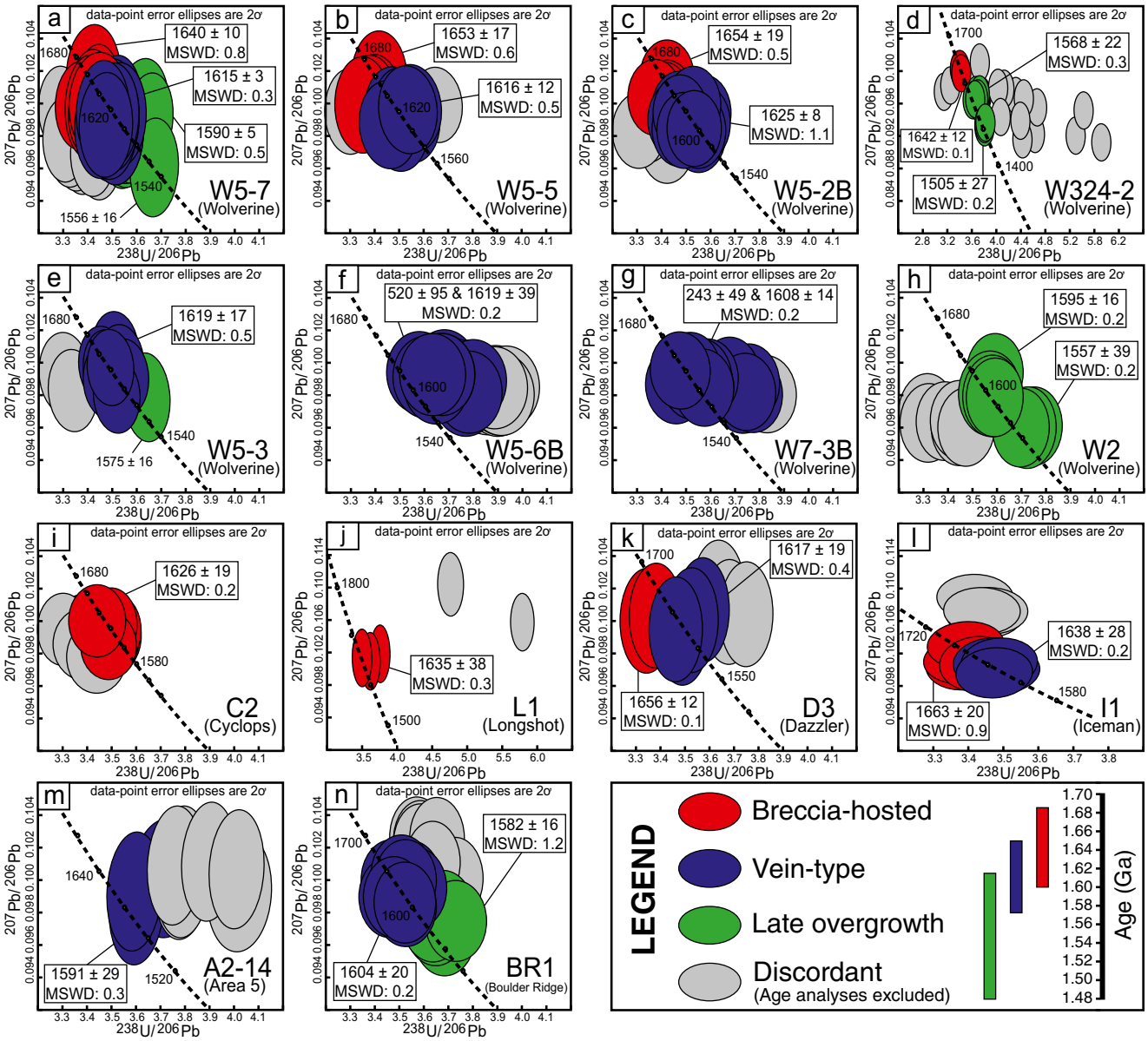

Fig. 13 **a**–**n** Tera–Wasserburg concordia diagrams for U–Pb isotope analysis of ore xenotime

also returned comparable U, Th, and Th/U values. In general, xenotime from across the deposit/prospects have U and Th contents in the range of several 1000 ppm U and 10s to 100 s of ppm Th, giving Th/U values of 0.01 to 0.04. Area 5 (mean U = 10,200 ppm, mean Th = 3800 ppm, Th/U = 0.01) and Longshot (mean U = 11,600 ppm, mean Th = 700 ppm, Th/U = 0.1) are comparatively rich in both U and Th and have more variable Th/U ratios. Common Pb contents tend to be very low, with 90% of the analyses containing less than 0.15 ppm ^{204}Pb. The few analyses that returned higher ^{204}Pb values (up to 1.8 ppm) all yielded very discordant ages (up to 40% discordance). With our discordance cutoff at 5% discordance, all of these analyses were not used from age calculations.

We have determined ages for all three xenotime types from the Wolverine deposit. Breccia-hosted xenotime analyzed in four of the eight samples from Wolverine returned the oldest ages of 1640 ± 10 Ma (sample W5-7: MSWD = 0.8, n = 8), 1653 ± 17 Ma (sample W5-5: MSWD = 0.6, n = 4), 1654 ± 19 Ma (sample W5-2B: MSWD = 0.5, n = 4), and 1642 ± 12 Ma (sample W324–2: MSWD = 0.1, n = 2) (Fig. 13a–d). Four samples of vein-type xenotime (samples W5-7, W5-5, W5-2B, and W5-3) produced almost entirely concordant ages of 1615 ± 3 Ma (MSWD = 0.3, n = 15), 1616 ± 12 Ma (MSWD = 0.5, n = 8), 1625 ± 8 Ma (MSWD = 1.1, n = 12), and 1619 ± 17 Ma (MSWD = 0.5, n = 10), respectively (Fig. 13a–c, e). Two other samples of vein xenotime (W5-6B and W7-3B) returned discordant ages with upper-intercept ages of 1619 ± 39 Ma (MSWD = 0.2, n = 12) and 1608 ± 14 Ma (MSWD = 0.2, n = 14) and lower-intercept ages of 520 ± 95 Ma (MSWD = 0.2) and 243 ± 49 Ma (MSWD = 0.2), respectively (Fig. 13f–g). Analysis of the late xenotime overgrowths returned multiple discrete younger ages of 1590 ± 5 Ma (MSWD = 0.5, n = 7) and 1556 ± 16 Ma (^{207}Pb/^{206}Pb age, n = 1) for sample W5-7, 1568 ± 22 Ma (MSWD = 0.3, n = 9) and 1505 ± 27 Ma (MSWD = 0.2, n = 3) for sample W324-2, 1575 ± 16 Ma (^{207}Pb/^{206}Pb age, n = 1) for sample W5-3, and 1595 ± 16 Ma (MSWD = 0.2, n = 4), and 1557 ± 39 Ma (MSWD = 0.2, n = 3) for sample W2 (Fig. 13a–h).

Breccia-hosted xenotime from Cyclops (sample C2), Longshot (sample L1), Dazzler (sample D3), and Iceman (sample I1) yielded age clusters of 1626 ± 19 Ma (MSWD = 0.2, n = 13), 1635 ± 38 Ma (MSWD = 0.3, n = 3), 1656 ± 12 Ma (MSWD = 0.1, n = 2), and 1663 ± 20 Ma (MSWD = 0.9, n = 4), respectively (Fig. 13i–l). Samples D3 and I1 also contain a crosscutting xenotime vein that returned age populations of 1617 ± 19 Ma (MSWD = 0.4, n = 4) and 1638 ± 28 Ma (MSWD = 0.2, n = 4). These latter ages are within uncertainty of ages determined for vein-type xenotime from Area 5 (sample A2-14, 1591 ± 29 Ma, MSWD = 0.3, n = 3) and Boulder Ridge (sample BR1, 1604 ± 20 Ma, MSWD = 0.2, n = 9) (Fig. 13m, n). Finally, euhedral xenotime overgrowths from sample BR1 gave an age cluster of 1582 ± 16 Ma (MSWD = 1.2, n = 5).

Collectively, U–Pb ages for various stages of xenotime from all deposits and prospects examined are between ca. 1650 Ma and ca. 1510 Ma (Figs. 13 and 14). Breccia-hosted xenotime (X1) dated from Wolverine, Cyclops, Dazzler, Iceman, and Longshot yielded concordant ages between ca. 1650 to ca. 1620 Ma. Assuming a single age event, these data produce a weighted mean age of 1646 ± 9 Ma (MSWD = 2.0). The vein-type xenotime (X2) present in most deposits/prospects returned mainly concordant, but slightly younger ages at ca. 1620 Ma, albeit with some overlap within uncertainty of the breccia-hosted xenotime age. Nevertheless, considering the textural observation of vein-type xenotime forming after the breccia xenotime, we are confident that we can treat the vein-type xenotime analyses as a separate younger event. The weighted mean of the vein xenotime data is 1615 ± 4 Ma (MSWD = 1.5). Multiple younger ages were generated from xenotime (X3) overgrowths from Wolverine and Boulder Ridge that extend from ca. 1600 to ca. 1500 Ma (Fig. 13). Many of these analyses are discordant, likely due to Pb loss, in which case the upper intercept is taken to be the crystallization age. The lower-intercept ages reported from samples W5-6B (ca. 520 Ma) and W7-3B (ca. 240 Ma) are similar to lower-intercept ages found for detrital zircons from the BRM (Nazari-Dehkordi et al. 2017) and are attributed to disturbance during the Alice Springs Orogeny (450–300 Ma; Raimondo et al. 2011).

Discussion

Mineralization style

Field observations and core log datasets indicate remarkable similarities between different HREE deposits/prospects across the NAHREY mineral field. All of the deposits/prospects have a similar ore mineralogy composed entirely of xenotime and florencite, and all are associated with an intense syn-ore quartz and white mica alteration. Mineralization is clearly of hydrothermal origin and mainly occurs along steeply dipping faults and major structures of variable orientation and close to regional unconformities, in most cases between the BRM and overlying Birrindudu Group sandstones. We propose that these structures acted as fluid pathways that witnessed large fluid fluxes, alongside which a breccia core of high-grade ore is surrounded commonly by a halo of lower grade ore, as is typical of vein-type mineralization. In such systems, orebodies sharing similar geological setting, ore-associated alteration and mineralogy, emplacement age, and structural controls can be considered as discrete parts of a larger mineralizing system with a common fluid source (e.g., unconformity-related U deposits of the Pine Creek Orogen; Skirrow et al.

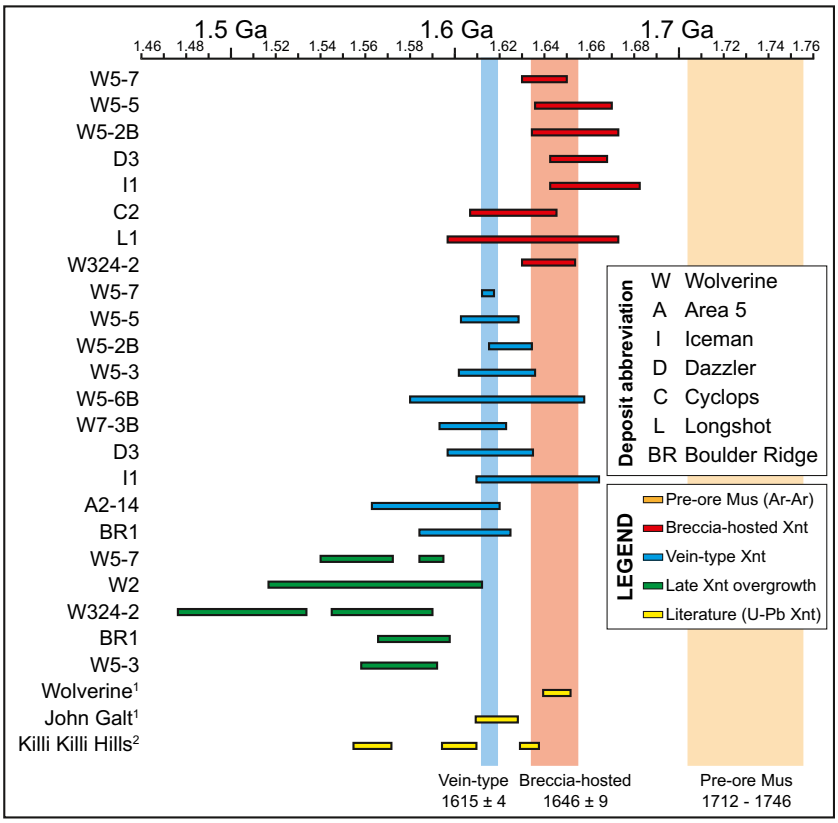

Fig. 14 Time plot of xenotime U–Pb ages for seven HREE deposits/prospects dated here, as well as from the literature (1 = Morin-Ka et al. 2016; 2 = Vallini et al. 2007). Also included is the Ar–Ar age range of the pre-ore muscovite (see Table 2 for more details). Note: the main stage of the HREE mineralization across the Tanami region is between 1.65 and 1.60 Ga, significantly younger than the pre-ore muscovite

2016 and references therein). In particular, structural correlation of most of the deposits/prospects of the Tanami region with the BRD supports a large hydrothermal mineralizing system. The variability in size of the HREE deposits/prospects is likely linked to fluid flux, which, at least in part, relates to the dilatancy and permeability of each individual fault system. For example, the largest known deposit, Wolverine, is located at the conjunction of two major faults (Fig. 4), where sufficient space accommodation allowed large fluxes (and mixing, see below) of fluids.

The HREE mineralization in the NAHREY mineral field is accommodated completely within metasedimentary rocks with no apparent link to magmatism or surficial process and, hence, is unlike other REE ore styles (Nazari-Dehkordi et al. 2018). This also includes the John Galt prospect from the Halls Creek Orogen (see Fig. 1) hosted by the metasedimentary rocks of the Red Rock Basin adjacent to an unconformity with older metamorphic rocks where mineralization crops out as networks of quartz–xenotime veins along major N–S-oriented faults and, most distinctively, along a ca. 100-m-high ENE-trending escarpment. The simple ore mineralogy of the NAHREY deposits/prospects also contrasts with the complex ore mineralogy of most other REE deposits (e.g., Weng et al. 2015). Although the HREE deposits/prospects studied here are restricted to northern Australia, the HREE mineralization of the Maw Zone, Canada, is directly comparable to the NAHREY mineralization. The Maw Zone consists of hydrothermal xenotime hosted within brecciated sandstones close to the Archean–Proterozoic unconformity in the Athabasca Basin (Quirt et al. 1991; Pan et al. 2013; Rabiei et al. 2017). Anomalous REE concentrations associated with hydrothermal alteration near regional unconformities have also been reported from the McArthur Basin of northern Australia and the Athabasca and Thelon Basins of Canada (Fayek and Kyser 1997; Davis et al. 2011; Orth et al. 2014). Xenotime- and florencite-rich quartz veins also occur within altered metasedimentary rocks of the subpolar Urals (Repina 2010). Accordingly, these reports indicate that there may be a global distribution for this particular ore style.

Temporal evolution of mineralization and relationship to regional-scale tectonics

Collectively, the ages of hydrothermal xenotime from seven HREE deposits/prospects in the Tanami region span a range of ca. 150 m.y, from ca. 1650 to ca. 1500 Ma (Fig. 14). This age range is interpreted to reflect multiple episodes of xenotime growth, and probably dissolution and regrowth, during both regional metamorphism and hydrothermal alteration.

1710–1740 Ma metamorphism

The pre-ore (M1) white mica $^{40}Ar/^{39}Ar$ ages of ca. 1710–1740 Ma reported for Wolverine and Area 5 (Table 2) is interpreted to record the timing of regional (largely lower

greenschist grade) metamorphism in the region. Our ages are comparable to numerous $^{40}Ar/^{39}Ar$ ages for the Tanami region (e.g., Dead Bullock Formation: ca. 1718 Ma, Li et al. 2014), and Halls Creek Orogen (e.g., Mabel Downs Tonalite: ca. 1705 Ma, Bodorkos and Reddy 2004). These ages are also in agreement with the xenotime ages reported from Pine Creek Orogen (Union Reefs Au deposit: 1701 ± 13 Ma, Sener 2004) and Kimberley Basin (Pentecost Sandstone: 1704 ± 14 Ma, Warton Sandstone: 1704 ± 7 Ma, McNaughton et al. 1999). Generally, ca. 1720 Ma is interpreted to correlate with the Strangways Orogeny (Fraser 2002), which was a major episode of high-grade metamorphism, west-directed thrusting and hydrothermal fluid circulation in the eastern part of the Arunta Block (Maidment et al. 2005).

Main HREE mineralization stage (1650–1600 Ma)

The major REE mineralization event producing the breccia ore is constrained to 1646 ± 9 Ma for most of the studied deposits/prospects, including Wolverine (Fig. 14). This age is indistinguishable from a previously-reported age on Wolverine (1646 ± 5 Ma) by Morin-Ka et al. (2016), and is also within error of the age of the Killi Killi Hills xenotime hosted within the Birrindudu Group sandstones (1633 ± 4 Ma, but up to 1639 Ma, Vallini et al. 2007). A well-constrained xenotime age of 1615 ± 4 Ma (Fig. 14) is also inferred for the vein-type HREE mineralization at Wolverine and several other deposits/prospects (Area 5, Iceman, Dazzler, Boulder Ridge). This age also compares well to the age previously reported from John Galt (1619 ± 9 Ma, Morin-Ka et al. 2016), suggesting that the hydrothermal activity responsible for vein formation was a regional scale event that extended from Halls Creek Orogen to the Tanami region. The younger age for vein-type xenotime compared to breccia-hosted xenotime also conforms to petrographic observations that quartz-xenotime veins crosscut the preexisting breccia-hosted xenotime (Fig. 9a–e).

The period around 1650 Ma that records the bulk of the HREE mineralization represents a time of complex geological activity in the North Australian Craton. Within this timeframe, the Mount Isa Inlier, lying on the eastern margin of the North Australian Craton, underwent major sedimentation (e.g., Soldiers Cap Group, Young Australia Group, Mount Albert Group, Foster and Austin 2008; Mount Isa Group and McNamara Group; Page et al. 2000), magmatism (e.g., the 1670–1650 Ma Sybella Batholith and Ernest Henry Diorite, Page et al. 2000) and base metal mineralization (Dugald River, Cannington, Mount Isa, Hilton-George Fisher, and McArthur River deposits all formed between 1665 to 1640; Page et al. 2000). These ages are broadly correlated to the ca. 1650 Ma assembly of the North Australian Craton and Laurentia (Pisarevsky et al. 2014), both of which subsequently underwent crustal extension at ca. 1640 Ma and re-assembly at ca. 1620 Ma during the Isan Orogeny (Gibson et al. 2017). Concurrently, collision of the Arunta Inlier with the Warumpi Province along the southern margin of the North Australian Craton during the Liebig Orogeny caused significant magmatism (1644 Ma Kakalyi Gneiss, Wyborn et al. 1998; and 1635 Ma Andrew Young Igneous Complex, Young et al. 1995) and metamorphism (e.g., ca. 1640–1635 Ma Yaya Metamorphic Complex, Scrimgeour et al. 2005; ca. 1615 Ma Iwupataka Metamorphic Complex, Zhao and Bennett 1995).

The broadly coeval collisions of the North Australian Craton with the Arunta Inlier to the south and Laurentia to the east caused abrupt changes in the apparent polar wander path of the North Australia Craton at ca. 1650 Ma and ca. 1640 Ma (Idnurm 2000). Although distal from these tectonic and magmatic events, we suggest that associated far-field effects caused faulting and large-scale fluid flow in the northern Tanami and Halls Creek zones, which provided suitable conditions for formation of HREE mineralization. A similar suggestion has been proposed for the base metal (e.g., Gibson et al. 2017), and uranium (e.g., ca. 1680 Ma Jabiluka and ca. 1640 Ma Nabarlek, Polito et al. 2005) deposits of the North Australia Craton.

Post ore stages (1600–1500 Ma)

The latest phase of the HREE mineralization, from ca. 1600 to ca. 1500 Ma (Fig. 14), relates primarily to xenotime overgrowths on preexisting xenotime. Two age populations of the xenotime from Killi Killi Hills within the Birrindudu Group sandstones (1602 ± 5 Ma and 1564 ± 8, Vallini et al. 2007), also fall into this ca. 100 m.y. timespan. The xenotime overgrowths likely formed by the relatively minor dissolution and subsequent overgrowth of earlier xenotime during a series of deformation/fluid events that postdate the main mineralization stage. The 1600–1500 Ma timespan of the late xenotime overgrowths corresponds well to far field tectonic events including the crustal shortening associated with the Isan Orogeny in the North Australian Craton that continued until ca. 1500 Ma (Gibson et al. 2017), and the Chewings Orogeny in the Arunta Inlier (ca. 1600–1525 Ma, Collins et al. 1995; Vallini et al. 2007). These major tectonic events resulted in substantial magmatism and metamorphism in both the Arunta Inlier (Zhao and Bennett 1995 and references therein) and the Mount Isa Inlier (Page and Sun 1998 and references therein). We suggest that further reworking of the North Australian Craton during the Isan Orogeny and the Chewings Orogeny was likely responsible for the formation of this younger generation of xenotime.

Implications of a prolonged temporal evolution

The total geochronological dataset implies that evolution of mineralization in the NAHREY mineral field was a prolonged

and multi-stage process extending from ca. 1650 down to ca. 1500 Ma (Fig. 14). Such long-lived episodic growth of REE-bearing minerals have been reported from REE deposits worldwide (ca. 1520 to ca. 350 Ma for the Nolans Bore REE deposit, Huston et al. 2016; ca. 1370 to ca. 815 Ma for the Gifford Creek Carbonatite Complex, Slezak and Spandler 2019; ca. 1300 to ca. 400 Ma for the Bayan Obo deposit, Song et al. 2018). Similarly, U deposits tend to undergo intermittent stages of mineralization and remobilization over timespans of several 100 m.y. to over 1 b.y. (ca. 1590 to ca. 500 Ma Olympic Dam, Cherry et al. 2018; ca. 1680 to ca. 800 Ma Jabiluka, Polito et al. 2005; ca. 1680 to ca. 470 Ma Ranger, Skirrow et al. 2016; ca. 1740 to ca. 1470 Ma Mary Kathleen, Oliver et al. 1999; ca. 1590 to ca. 850 Ma Athabasca Basin, Alexandre et al. 2009). Such common features between REE and U deposits suggest that radiogenic isotopic systems were sporadically disturbed, with the age of disturbance at least partly controlled by radiogenic heat production and mineral recrystallization, resulting in the development of complex orebodies involving several stages of mineralization (see also Huston et al. 2016). In this case, REE and U ore minerals may be especially effective as recorders of postformation thermotectonic events due to their susceptibility to hydrothermal recrystallization and an inherent high level of radiogenic heat production due to their high U and Th contents.

Toward an ore genesis model

Traditionally, alkaline and peralkaline igneous complexes have been linked with REE enrichment processes (e.g., Strange Lake, Salvi and Williams-Jones 2006; Thor Lake, Sheard et al. 2012). Indeed, mid-Paleoproterozoic (1870 to 1790 Ma) igneous rocks are a major component of the Tanami region and Browns Range Dome (Page et al. 1995; Cross and Crispe 2007), prompting Cook et al. (2013) to suggest a magmatic source for the HREE mineralization. However, the age dataset reported here demonstrates that the main stage (ca. 1650 to ca. 1600 Ma) of the HREE mineralization in the NAHREY mineral field was not coincident with any known local or regional magmatic activity. Magmatic rocks of coeval age are limited only to the Mount Isa Inlier well to the east and the Arunta Inlier far to the south (Fig. 15). Furthermore, the unradiogenic Nd isotopic composition of the orebodies is inconsistent with that of any igneous rocks from across the North Australian Craton (Nazari-Dehkordi et al. 2018).

The geological relationships of the ore and petrographic textures of the ore minerals and associated quartz veins all suggest a hydrothermal origin for the HREE mineralization. Indeed, the mineralization setting of the NAHREY mineral field is remarkably similar to that of unconformity-related U deposits of the Athabasca Basin and the Pine Creek Orogen; both ore styles are structurally controlled and are associated with regional unconformities between Paleoproterozoic sedimentary packages and underlying Archean basement dominated by metasedimentary rocks (e.g., Richard et al. 2016). There are also similarities in ore-related alteration styles, with intense white mica alteration zones intimately associated with many unconformity-related U deposits (e.g., Alexandre et al. 2005). Available age datasets place initial U deposition within the Pine Creek Orogen at 1737 ± 20 Ma (Ranger 1: Ludwig et al. 1987), with the main stages of U mineralization constrained to 1700–1680 Ma (Polito et al. 2004, 2005, 2011) and 1650–1600 Ma (Maas 1989; Polito et al. 2004; Clauer et al. 2015; Skirrow et al. 2016). The latter age range overlaps the 1600–1590 Ma age of the bulk of the U mineralization reported from the Athabasca Basin (Alexandre et al. 2009). Collectively, the U ore formation in the Athabasca Basin and Pine Creek Orogen was in part coeval with the main stage (ca. 1650–1600 Ma) of the HREE mineralization presented here (Fig. 14).

Given these similarities in geological setting, aspects of ore genesis models for unconformity-related U deposits are likely to be applicable for mineralization in the NAHREY mineral field. The most accepted genetic models for the unconformity-related U deposits involve mixing of an oxidizing basinal fluid with a reducing fluid, with U being sourced either from the overlying sandstones (e.g., Kyser et al. 2000) or the underlying basement (e.g., Athabasca Basin: Mercadier et al. 2013 and references therein; Pine Creek Orogen: Skirrow et al. 2016 and references therein). Similarly, we suggest that mineralization in the NAHREY mineral field was produced by mixing of hydrothermal fluids along subvertical faults near the regional unconformity between the underlying Archean basement rocks (mainly the BRM) and overlying Proterozoic sandstones. Fluid mixing not only conforms to the structural and geological setting but is considered essential to explain the concentration of REE phosphate minerals in the ore zones. Xenotime has extremely low solubility in hydrothermal fluids (Gysi et al. 2015; Migdisov et al. 2016), so hydrothermal transport of REE + Y and P to the site of mineralization requires separate fluids. Nazari-Dehkordi et al. (2018) indicated that xenotime orebodies from across the NAHREY mineral field share a similar highly unradiogenic Nd isotopic composition with the Archean basement (BRM), which is very different from that of the unconformably overlying Birrindudu Group sandstones, demonstrating that REE + Y were sourced from the basement in acidic, highly saline fluids. Such fluid compositions may be effective at transporting REE + Y (e.g., Migdisov et al. 2016) and are entirely consistent with the formation of halogen-rich syn-ore white mica (Fig. 12c) alteration replacing K-feldspar (Fig. 6) in the ore zones. The relatively high F of these basinal brines may reflect the low Ca nature of the metamorphic basement rocks (Nazari-Dehkordi et al. 2017), conditions that are favorable for producing high-fluoride groundwaters (Chae et al. 2007).

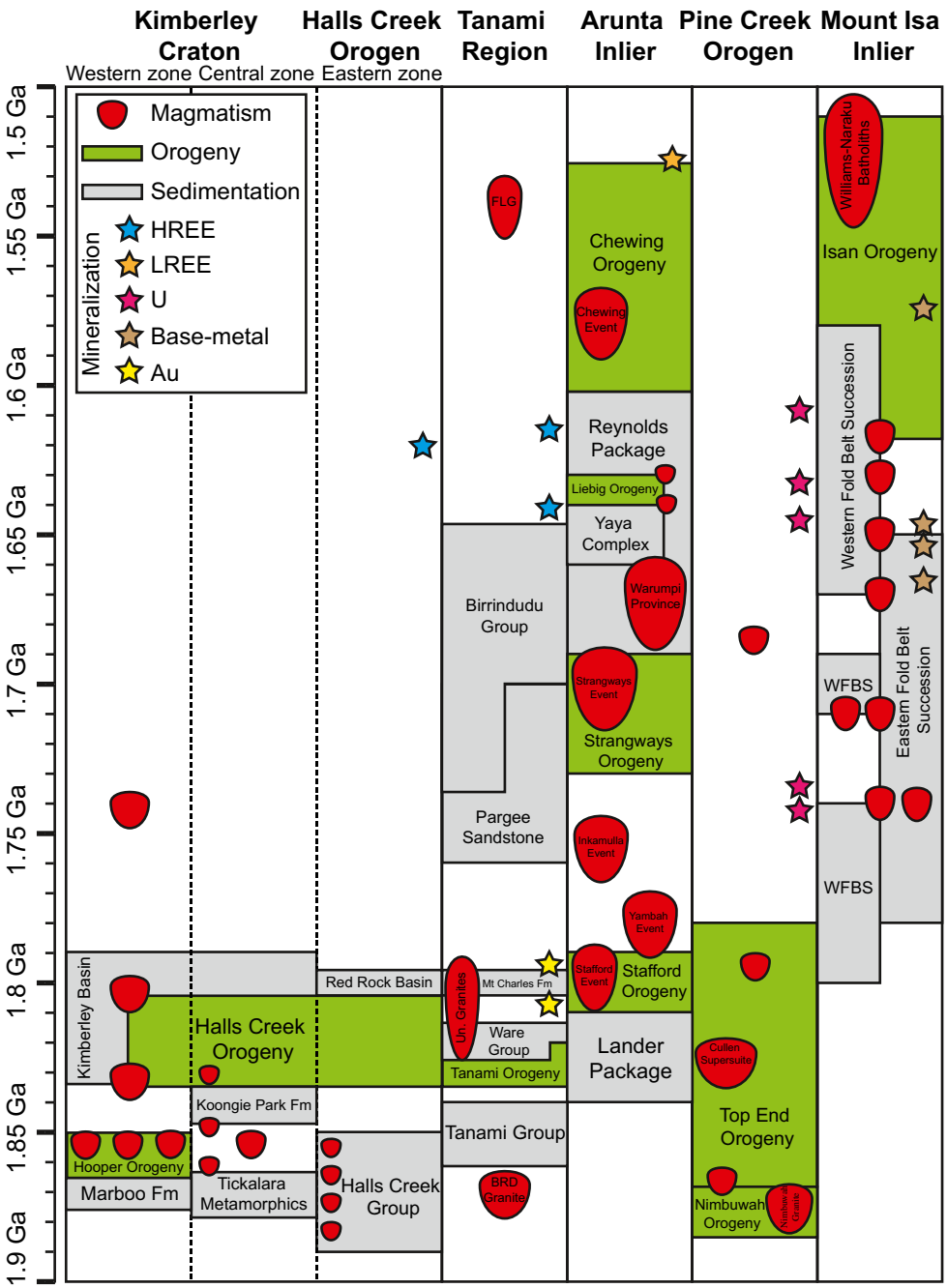

Fig. 15 Time–space plot of the 1.9–1.5 Ga events in the North Australian Craton. Data sources are Gibson et al. (2017) for the Mount Isa Inlier, Mercadier et al. (2013) for the Pine Creek Orogen, Scrimgeour et al. (2005) for the Arunta Inlier, Bagas et al. (2008) for the Tanami region, Sheppard et al. (1999) for the Halls Creek Orogen, and Lan and Chen (2012) for the Kimberley Craton. Note: the timing of the HREE mineralization in the Tanami region does not correlate to any local magmatism

The phosphorus for ore mineral formation is proposed to have been leached from the overlying apatite-bearing Birrindudu Group sandstones. Detrital apatite in the Birrindudu Group sandstones originated from the ca. 1.83 to ca. 1.79 Ga granites in the Tanami region (Crispe et al. 2007). Phosphate dissolution was likely driven via low-pH meteoric fluids circulating through the Birrindudu Group sandstones, as has been reported for other sandstone units (e.g., Morton 1986). The bulk of the HREE mineralization (at 1.65–1.60 Ga) formed in fault zones where upwelling BRM-derived REE + Y-bearing fluid mixed with P-bearing fluid derived from the Birrindudu Group sandstones. Mixing of fluids of varying salinity is also consistent with the compositions of fluid inclusions trapped within ore-associated quartz (Nazari-Dehkordi 2018). Temperatures of ore formation are expected to be between 150 and 350 °C (Nazari-Dehkordi et al. 2018) based on alteration mineral assemblages and fluid inclusion data (Nazari-Dehkordi 2018; Richter et al. 2018). These temperature conditions are consistent with the preservation of primary Ar of the pre-ore (M1) muscovite (indicating $T < 420$ °C; Harrison et al. 2009) and the formation of K-deficient syn-ore (M2) mica (Fig. 12b), which is only

expected to be stable below 400 °C (Rosenberg 2002). Under these conditions, xenotime (and florencite) solubility in fluids is extremely low, so fluid mixing would result in very efficient precipitation of ore minerals in fault zones. HREE (+Y) are considered to be the most insoluble of the REE (e.g., Williams-Jones et al. 2012) and, hence, would have been most easily lost from the reacting fluid. In this case, it is likely that some portion of LREE remained dissolved in the fluids to be transported out of the ore zone.

The Area 5 orebody formed during the main stage of the REE mineralization but is distinct from other deposits/prospects as it is dominated by florencite, with subordinate xenotime, and hence, is relatively LREE rich (Fig. 5a). We propose that this LREE flavor of Area 5 may reflect more comprehensive precipitation of the dissolved load of REE from the fluids or, more likely, that Area 5 formed from hydrothermal fluids that had already seen partial and preferential HREE depletion via prior xenotime precipitation. A similar process was proposed by Williams-Jones et al. (2015) to explain HREE- and LREE-rich zones of the Lofdal HREE deposit in Namibia. In this case, Area 5 can be considered to be "distal" to the other HREE-rich orebodies (e.g., Wolverine), in terms of evolution of the hydrothermal system.

In general, our ore genesis model agrees with the model proposed by Rabiei et al. (2017) for the Maw Zone unconformity-related xenotime deposit of Canada, although the Maw Zone is enriched in tourmaline and likely formed at shallower crustal depths than the NAHREY deposits. Where the NAHREY deposits (and Maw Zone) are distinct from unconformity-related U deposits is their association with significant hydrothermal quartz, lack of chlorite, and relatively low concentrations of U. Given the similarities in geological settings, these differences may be ultimately related to hydrothermal fluid compositions and ore precipitation mechanisms. Reaction of oxidized U^{6+}-bearing brines with the reductants such as Fe^{2+}-bearing chlorite is widely considered to be a crucial mechanism for ore formation in unconformity-related U deposits (e.g., Fayek and Kyser 1997; Alexandre et al. 2005). In contrast, redox changes are not expected to play any significance role in formation of REE ore in the NAHREY mineral field, as HREE are insensitive to changes in redox state. Instead, fluid mixing and associated increase in pH as indicated by syn-ore white mica is proposed as the trigger for REE phosphate ore formation.

Exploration implications

Identification of the ore-associated structures has significant implications for exploration, particularly for structurally controlled regional-scale orebody occurrences, such as in the NAHREY mineral field. The ore-bearing structures distributed within and around the BRD are of variable strike, suggesting that the HREE mineralization was associated with major faulting and/or reactivating of older faults in the basement. Conjugate fracture sets, especially involving E–W-striking structures, tend to be favored site for mineralization (e.g., Wolverine). These structures are typical of the dome-related structures (Cooper et al. 2006), so we suggest that doming of the BRD may have provided suitable structural architecture for the HREE mineralization. Hence, the dome-related structures, particularly E–W-trending faults, can be considered as potential exploration targets for the discovery of further HREE orebodies.

The spatial and genetic association between regional unconformity structures and mineralization in the NAHREY mineral field raises the potential for further HREE mineralization to be found associated with other regional unconformities within intercontinental sedimentary basins. Indeed, a number of the HREE deposits/prospects studied here (Cyclops and Dazzler; see Fig. 2b) are hosted directly along the unconformity structure. As mineralization requires a source of P, overlying sedimentary units rich in phosphate could also be considered as potential exploration targets for mineralization. Source rocks for ore metals need not be particularly REE-rich (see Nazari-Dehkordi et al. 2018) but should be depleted in P and Ca to avoid fluorite and/or apatite saturation that would serve to greatly restrict REE mobility.

The strong association of U with HREE (Fig. 5) has proved very useful for exploration using remotely sensed radiometric surveys. Here, we recognize ore-associated white mica alteration compositions (phengite–illite; Fig. 12) that are quite distinct from the pre-ore metamorphic muscovite of the region. This distinctive ore-associated mica is potentially well resolved by hyperspectral remote sensing techniques (Van der Meer et al. 2012), meaning hyperspectral mapping combined with regional radiometric surveys has great potential to be an effective regional-scale exploration tool.

Conclusion

Major findings of this study include the following:

1. HREE mineralization in the NAHREY mineral field is of hydrothermal origin. Ore formation was a multistage process that primarily occurred between 1.65 and 1.60 Ga, with several subsequent episodes of xenotime growth and regrowth.
2. Ore formation is not related to any local or regional magmatism but coincided with the initiation of the Isan and Liebig Orogenies to the west and south, respectively. Far-field stresses from these events are the potential drivers of large-scale fluid flow leading to the ore formation.
3. We propose an ore genesis model that involves mixing of discrete hydrothermal fluids that separately carried REE +

Y and P from the BRM and the overlying Birrindudu Group sandstones, respectively. Ore formation is best developed at fault intersections and along the unconformity surface where fluid mixing was facilitated.

Acknowledgments We thank David Huston for editorial handling and two anonymous reviewers for their insightful comments.

Funding information This work was supported by Northern Minerals Ltd. and an ARC Future Fellowship (FT 120100198) to CS.

References

Aleinikoff JD, Selby D, Slack JF, Day WC, Pillers RM, Cosca MA, Seeger CM, Fanning CM, Samson IM (2016) U-Pb, Re-Os, and Ar/Ar geochronology of rare earth element (REE)-rich breccia pipes and associated host rocks from the Mesoproterozoic Pea Ridge Fe-REE-Au deposit, St. Francois Mountains, Missouri. Econ Geol 111: 1883–1914

Alexandre P, Kyser K, Polito P, Thomas D (2005) Alteration mineralogy and stable isotope geochemistry of Paleoproterozoic basement-hosted unconformity-type uranium deposits in the Athabasca Basin, Canada. Econ Geol 100:1547–1563

Alexandre P, Kyser K, Jiricka D (2009) Critical geochemical and mineralogical factors for the formation of unconformity-related uranium deposits: comparison between barren and mineralized systems in the Athabasca Basin, Canada. Econ Geol 104:413–435

Bagas L, Huston DL, Anderson J, Mernagh TP (2007) Paleoproterozoic gold deposits in the Bald Hill and Coyote areas, Western Tanami, Western Australia. Mineral Deposita 42:127–144

Bagas L, Bierlein FP, English L, Anderson J, Maidment D, Huston DL (2008) An example of a Palaeoproteozoic back-arc basin: petrology and geochemistry of the ca. 1864 Ma Stubbins Formation as an aid towards an improved understanding of the Granites-Tanami Orogen, Western Australia. Precambrian Res 166:168–184

Blake DH, Hodgson IM, Smith PA (1975) Geology of the Birrindudu and Tanami 1:2500000 sheet areas, Northern Territory. Bureau of Mineral Resources, Australia, Report 174

Bodorkos S, Reddy SM (2004) Proterozoic cooling and exhumation of the northern central Halls Creek Orogen, Western Australia: constraints from a reconnaissance $^{40}Ar/^{39}Ar$ study. Aust J Earth Sci 51:591–609

Busch JP, van der Pluijm BA, Hall CM, Essene EJ (1996) Listric normal faulting during postorogenic extension revealed by $^{40}Ar/^{39}Ar$ thermochronology near the Robertson Lake shear zone, Grenville Orogen, Canada. Tectonics 15:387–402

Chae GT, Yun ST, Mayer B, Kim KH, Kim SY, Kwon JS, Kim K, Koh YK (2007) Fluorine geochemistry in bedrock groundwater of South Korea. Sci Total Environ 385:272–283

Chakhmouradian AR, Zaitsev AN (2012) Rare earth mineralization in igneous rocks: sources and processes. Elements 8:347–353

Cherry AR, Kamenetsky VS, McPhie J, Thompson JM, Ehrig K, Meffre S, Kamenetsky MB, Krneta S (2018) Tectonothermal events in the Olympic IOCG Province constrained by apatite and REE-phosphate geochronology. Aust J Earth Sci 65:643–659

Clark AB, Blockley JG (1960) A report on a geological reconnaissance, Billiluna area (authority to prospect 769, Northern Territory). Open File, New Consolidated Gold Fields Pty Ltd, p 1–9

Clauer N, Mercadier J, Patrier P, Laverret E, Bruneton P (2015) Relating unconformity-type uranium mineralization of the Alligator Rivers Uranium Field (Northern Territory, Australia) to the regional Proterozoic tectono-thermal activity: an illite K–Ar dating approach. Precambrian Res 269:107–121

Collins WJ, Williams IS, Shaw SE, McLaughlin NA (1995) The age of the Ormiston Pound Granite: implications for Mesoproterozoic evolution of the Arunta Inlier, central Australia. Precambrian Res 71: 91–105

Cook NJ, Ciobanu CL, O'Rielly D, Wilson R, Das K, Wade B (2013) Mineral chemistry of rare earth element (REE) mineralization, Browns Ranges, Western Australia. Lithos 172-173:192–213

Cooper SP, Goodwin LB, Lorenz JC (2006) Fracture and fault patters associated with basement-cored anticlines: the example of Teapot Dome, Wyoming. Am Assoc Pet Geol Bull 90:1903–1920

Crispe A, Vandenberg L (2005) Geology of the Tanami region, Northern Territory. Northern Territory Geol Surv Bull

Crispe AJ, Vandenberg LC, Scrimgeour I (2007) Geological framework of the Archaean and Palaeoproterozoic Tanami region, Northern Territory. Mineral Deposita 42:1–26

Cross A, Crispe A (2007) SHRIMP U-Pb analyses of detrital zircon: a window to understanding the Paleoproterozoic development of the Tanami region, northern Australia. Mineral Deposita 42:27–50

Davis WJ, Gall Q, Jefferson CW, Rainbird RH (2011) Fluorapatite in the Paleoproterozoic Thelon Basin: structural-stratigraphic context, in-situ ion microprobe U-Pb ages, and fluid flow history. Geol Soc Am Bull 123:1056–1073

Dawson GC, Krapez B, Fletcher IR, McNaughton NJ, Rasmussen B (2003) 1.2 Ga thermal metamorphism in the Albany–Fraser Orogen of Western Australia: consequence of collision or regional heating by dyke swarms? J Geol Soc 160:29–37

Fayek M, Kyser TK (1997) Characterization of multiple fluid-flow events and rare-earth element mobility associated with formation of unconformity-type uranium deposits in the Athabasca Basin Saskatchewan. Can Mineral 35:627–658

Fletcher IR, McNaughton NJ, Aleinikoff JA, Rasmussen B, Kamo SL (2004) Improved calibration procedures and new standards for U-Pb and Th-Pb dating of Phanerozoic xenotime by ion microprobe. Chem Geol 209:295–314

Foster DRW, Austin JR (2008) The 1800-1610 Ma stratigraphic and magmatic history of the Eastern Succession, Mount Isa Inlier, and correlations with adjacent Paleoproterozoic terranes. Precambrian Res 163:7–30

Fraser G (2002) geochronology of Tanami ores and host rocks. In: Munson TJ, Scrimgeour I (eds) Northern Territory Geol Surv Bull

Gibson GM, Hutton LJ, Holzschuh J (2017) Basin inversion and supercontinent assembly as drivers of sediment-hosted Pb–Zn mineralization in the Mount Isa region, northern Australia. J Geol Soc 174: 773–786

Goodenough KM, Wall F, Merriman D (2018) The rare earth elements: demand, global resources, and challenges for resourcing future generations. Nat Resour J 27:201–216

Gysi AP, Williams-Jones AE, Harlov D (2015) The solubility of xenotime-(Y) and other HREE phosphates ($DyPO_4$, $ErPO_4$ and $YbPO_4$) in aqueous solutions from 100 to 250°C and sat. Chem Geol 41:83–95

Harrison TM, Celerier J, Aikman AB, Hermann J, Heizler MT (2009) Diffusion of ^{40}Ar in muscovite. Geochim Cosmochim Acta 73: 1039–1051

Hendrickx MA, Slater K, Crispe AJ, Dean AA, Vandenberg LC, Smith JB (2000) Paleoproterozoic stratigraphy of the Tanami region: regional correlations realisation preliminary results. Northern Territory Geol Surv Bull

Huston DL, Maas R, Cross A, Hussey KJ, Mernagh TP, Fraser G, Champion DC (2016) The Nolans Bore rare-earth element-phosphorus-uranium mineral system: geology, origin and post-depositional modifications. Mineral Deposita 51:797–822

Idnurm M (2000) Towards a high resolution late Palaeoproterozoic-earliest Mesoproterozoic apparent polar wander path for northern Australia. Aust J Earth Sci 47:405–429

Keane SD, Dewolf CP, Essene EJ, Halliday AN, Hall CM, Cosca MA (2006) Isotopic constraints on the thermal history of the Wind River Range, Wyoming: implications for Archean metamorphism. Can J Earth Sci 43:1511–1532

Korzhinskii DS (1970) Theory of metasomatic zoning. Clarendon, Oxford, 162 p

Kyser K, Hiatt EE, Renac C, Durocher K, Holk G, Deckart K (2000) Diagenetic fluids in paleo- and meso-proterozoic sedimentary basins and their implications for long protracted fluid histories. In: Kyser TK (ed) Fluids and basin evolution. Min Assoc Can 28: 225–262

Lan Z-W, Chen Z-Q (2012) New xenotime ages obtained from the Paleoproterozoic Kimberley Group, NW Australia: implications for regional hydrothermal events. Aust J Earth Sci 59:119–133

Li B, Bagas L, Jourdan F (2014) Tectono-thermal evolution of the Palaeoproterozoic Granites–Tanami Orogen, North Australian Craton: implications from hornblende and biotite $^{40}Ar/^{39}Ar$ geochronology. Lithos 206:262–276

Ludwig KR (2009) User's manual for isoplot 3.70: a geochronological toolkit for Microsoft Excel. Berkeley Geochronology Center Special Publication No. 4

Ludwig KR, Grauch RI, Nutt CJ, Nash JT, Frishman D, Simmons KR (1987) Age of uranium mineralization at the Jabiluka and Ranger uranium deposits, Northern Territory, Australia: new U–Pb isotope evidence. Econ Geol 82:857–874

Maas R (1989) Nd–Sr isotopic constraints on the age and origin of unconformity-type uranium deposits in the Alligator Rivers uranium field, Northern Territory, Australia. Econ Geol 84:64–90

Maidment DW, Hand M, Williams IS (2005) Tectonic cycles in the Strangways Metamorphic Complex, Arunta Inlier, central Australia: geochronological evidence for exhumation and basin formation between two high-grade metamorphic events. Aust J Earth Sci 52:205–215

McNaughton NJ, Rasmussen B, Fletcher IR (1999) SHRIMP uranium-lead dating of diagenetic xenotime in siliciclastic sedimentary rocks. Science 285:78–80

Meert JG, Hargraves RB, van der Voo R, Hall CM, Halliday AN (1994) Paleomagnetic and $^{40}Ar/^{39}Ar$ studies of late Kibaran intrusives in Burundi, East Africa: implications for late Proterozoic supercontinents. J Geol 102:621–637

Meisel T, Schoner N, Paliulionyte V, Kahr E (2002) Determination of rare earth elements, Y, Th, Zr, Hf, Nb and ta in geological reference materials G-2, G-3, SCo-1 and WGB-1 by sodium peroxide sintering and inductively coupled plasma-mass spectrometry. Geostand Newslett 26:53–61

Mercadier J, Annesley IR, McKechnie CL, Bogdan TS, Creighton S (2013) Magmatic and metamorphic uraninite mineralization in the western margin of the trans-Hudson Orogen (Saskatchewan, Canada): a uranium source for unconformity-related uranium deposits? Econ Geol 108:1037–1065

Migdisov A, Williams-Jones AE, Brugger J, Caporuscio F (2016) Hydrothermal transport, deposition, and fractionation of REE: experimental data and thermodynamic calculations. Chem Geol 439: 13–42

Morin-Ka S, Beardsmore TJ, Hancock EA, Rasmussen B, Dunkley D, Muhling J, Zi J, Wilson R, Champion J (2016) Alteration and age of the browns range rare earth element deposits. Western Australian Department of Mines and Petroleum

Morton AC (1986) Dissolution of apatite in North Sea Jurassic sandstones: implications for the generation of secondary porosity. Clay Miner 21:711–733

Nazari-Dehkordi T (2018) The origin and evolution of heavy rare earth element mineralization in the Browns Range area, Northern Australia. PhD thesis, James Cook University, Australia

Nazari-Dehkordi T, Spandler C, Oliver NHS, Chapman J, Wilson R (2017) Provenance, tectonic setting and source of Archean metasedimentary rocks of the Browns Range Metamorphics, Tanami region, Western Australia. Aust J Earth Sci 64:723–741

Nazari-Dehkordi T, Spandler C, Oliver NHS, Wilson R (2018) Unconformity–related rare earth element deposits: a regional-scale hydrothermal mineralization type of northern Australia. Econ Geol 6:1297–1305

Northern Minerals (2018) Annual report to shareholders. http://northernminerals.com.au/investor-centre/#NaN

Oliver NHS, Bodorkos S, Nemchin AA, Kinny PD, Watt GR (1999) Relationships between zircon U–Pb SHRIMP ages and leucosome type in migmatites of the Halls Creek Orogen, Western Australia. J Petrol 40:1553–1575

Orth K, Meffre S, Davidson G (2014) Age and paragenesis of mineralization at Coronation Hill uranium deposit, Northern Territory, Australia. Mineral Deposita 49:595–623

Page RW, Sun SS (1998) Aspects of geochronology and crustal evolution in the Eastern Fold Belt, Mt Isa Inlier. Aust J Earth Sci 45:343–361

Page RW, Sun SS, Blake D, Edgecombe D, Pearcey D (1995) Geochronology of an exposed late Archean basement terrane in the Granites-Tanami region. Aust Geol Surv Org 22:21–22

Page RW, Jackson MJ, Krassay AA (2000) Constraining sequence stratigraphy in North Australian basins: SHRIMP U–Pb zircon geochronology between Mt Isa and McArthur River. Aust J Earth Sci 47: 431–459

Pan Y, Yeo G, Rogers B, Austman C, Hu B (2013) Application of radiation induced defects in quartz to exploration for uranium deposits: a case study of the Maw Zone, Athabasca Basin, Saskatchewan. Explor Min Geol 21:115–128

Pettke T, Oberli F, Audetat A, Guillong M, Simon AC, Hanley JJ, Klemm LM (2012) Recent developments in element concentration and isotope ratio analysis of individual fluid inclusions by laser ablation single and multiple collector ICP-MS. Ore Geol Rev 44:10–38

Pisarevsky SA, Elming SA, Pesonen LJ, Li ZX (2014) Mesoproterozoic paleogeography: supercontinent and beyond. Precambrian Res 244: 207–225

Polito PA, Kyser TK, Marlatt J, Alexandre P, Bajwah Z, Drever G (2004) Significance of alteration assemblages for the origin and evolution of the Proterozoic Nabarlek unconformity-related uranium deposit, Northern Territory, Australia. Econ Geol 99:113–139

Polito PA, Kyser TK, Thomas D, Marlatt J, Drever G (2005) Re-evaluation of the petrogenesis of the Proterozoic Jabiluka unconformity-related uranium deposit, Northern Territory, Australia. Mineral Deposita 40:238–257

Polito PA, Kyser TK, Alexandre P, Hiatt EE, Stanley CR (2011) Advances in understanding the Kombolgie Subgroup and unconformity-related uranium deposits in the Alligator Rivers Uranium Field and how to explore for them using lithogeochemical principles. Aust J Earth Sci 58:453–474

Quirt D, Kotzer T, Kyser TK (1991) Tourmaline, phosphate minerals, zircon and pitchblende in the Athabasca Group: Maw Zone and McArthur River areas: Saskatchewan Geological Survey Report 91.4:181–191

Rabiei M, Chi G, Normand C, Davis WJ, Fayek M, Blamey NJF (2017) Hydrothermal rare earth element (xenotime) mineralization at Maw Zone, Athabasca Basin, Canada, and its relationship to unconformity-related uranium deposits. Econ Geol 112:1483–1507

Raimondo T, Clark C, Hand M, Faure K (2011) Assessing the geochemical and tectonic impacts of fluid–rock interaction in mid-crustal shear zones: a case study from the intracontinental Alice Springs Orogen, central Australia. J Metamorph Geol 29:821–850

Repina SA (2010) Zoning and sectoriality of the florencite and xenotime group minerals from quartz veins, the Subpolar Urals. Geol Ore Deposit 52:821–836

Richard A, Cathelineau M, Boiron MC, Mercadier J, Banks DA, Cuney M (2016) Metal-rich fluid inclusions provide new insights into unconformity-related U deposits (Athabasca Basin and Basement, Canada). Mineral Deposita 51:249–270

Richter L, Diamond LW, Atanasova P, Banks DA, Gutzmer J (2018) Hydrothermal formation of heavy rare earth element (HREE)-xenotime deposits at 100 °C in a sedimentary basin. Geology. https://doi.org/10.1130/G39871.1

Rieder M, Cavazzini G, Yakonov YS, Frank-Kamenetskii VA, Gottard G, Guggenheim S, Koval PV, Muller G, Neiva MAR, Radoslovic EW, Robert JL, Sassi SP, Takeda H, Weiss Z, Wones DR (1999) Nomenclature of the micas. Mineral Mag 63:267–279

Rosenberg PE (2002) The nature, formation, and stability of end-member illite: a hypothesis. Am Mineral 87:103–107

Salvi S, Williams-Jones AE (2006) Alteration, HFSE mineralization and hydrocarbon formation in peralkaline igneous systems: insights from the Strange Lake Pluton, Canada. Lithos 91:19–34

Samson SD, Alexander ECJ (1987) Calibration of the interlaboratory $^{40}Ar/^{39}Ar$ dating standard, MMhb-1. Chem Geol 66:27–34

Scrimgeour IR, Kinny PD, Close DF, Edgoose CJ (2005) High-T granulites and polymetamorphism in the southern Arunta region, central Australia: evidence for a 1.64 Ga accretional event. Precambrian Res 142:1–27

Sener AK (2004) Characteristics, distribution and timing of gold mineralization in the Pine Creek Orogen, Northern Territory, Australia. PhD dissertation, University of Western Australia

Sheard ER, Williams-Jones AE, Heiligmann M, Pederson C, Trueman DL (2012) Controls on the concentration of zirconium, niobium, and the rare earth elements in the Thor lake rare metal deposit, Northwest Territories, Canada. Econ Geol 107:81–104

Sheppard S, Tyler IM, Griffin TG, Taylor WR (1999) Paleoproterozoic subduction-related and passive margin basins in the Halls Creek Orogen, northwest Australia. Aust J Earth Sci 46:679–690

Sheppard S, Rasmussen B, Muhling JR, Farrell TR, Fletcher IR (2007) Grenvillian-aged orogenesis in the Palaeoproterozoic Gascoyne Complex, Western Australia: 1030–950 Ma reworking of the Proterozoic Capricorn Orogen. J Metamorph Geol 25:477–494

Skirrow RG, Mercadier J, Armstrong R, Kuske T, Deloule E (2016) The ranger uranium deposit, northern Australia: timing constraints, regional and ore-related alteration, and genetic implications for unconformity-related mineralization. Ore Geol Rev 76:463–503

Slezak P, Spandler C (2019) Carbonatites as recorders of mantle-derived magmatism and subsequent tectonic events: an example of the Gifford Creek Carbonatite Complex, Western Australia. Lithos 328-329: 212–227

Song W, Xu C, Smith MP, Chakhmouradian AR, Brenna M, Kynicky J, Chen W, Yang Y, Deng M, Tang H (2018) Genesis of the world's largest rare earth element deposit, Bayan Obo, China: protracted mineralization evolution over ~1 b.y. Geology 46:323–326

Spandler C, Hammerli J, Sha P, Hilbert-Wolf H, Hu Y, Roberts E, Schmitz M (2016) MKED1: a new titanite standard for in situ analysis of Sm-Nd isotopes and U-Pb geochronology. Chem Geol 425: 110–126

Stern RA, Rayner N (2003) Ages of several xenotime megacrysts by ID-TIMS: potential reference materials for ion probe U–Pb geochronology. Geological Survey of Canada, Current Research 2003-F1; radiogenic age and isotopic studies. Report 16:1–7

Streepey MA, van der Pluijm BA, Essene EJ, Hall CM, Magloughlin JF (2000) Late Proterozoic (ca 930 Ma) extension in eastern Laurentia. Geol Soc Am Bull 112:1522–1530

Vallini DA, Groves DI, McNaughton NJ, Fletcher IR (2007) Uraniferous diagenetic xenotime in northern Australia and its relationship to unconformity-associated uranium mineralization. Mineral Deposita 42:51–64

Van Achterbergh E, Ryan CG, Jackson SE, Griffin WL (2001) Data reduction software for LA-ICP-MS. In: Sylvester PJ (ed) Laser ablation-ICP mass spectrometry in the earth sciences: principles and applications. Min Assoc Can 29:239–243

Van der Meer FD, Van der Werff HM, Van Ruitenbeek FJ, Hecker CA, Bakker WH, Noomen MF, Woldai T (2012) Multi-and hyperspectral geologic remote sensing: a review. Int J Appl Earth Obs Geoinf 14: 112–128

Weng Z, Jowitt SM, Mudd GM, Nawshad HA (2015) A detailed assessment of global rare earth element resources: opportunities and challenges. Econ Geol 110:1925–1952

Williams-Jones AE, Migdisov AA, Samson IM (2012) Hydrothermal mobilization of the rare earth elements—a tale of "Ceria" and "Yttria". Elements 8:355–360

Williams-Jones AE, Wollenberg R, Bodeving S (2015) Hydrothermal fractionation of the rare earth elements and the genesis of the Lofdal REE deposit, Namibia. Symposium on critical and strategic materials. British Columbia Geol Surv 2015–3

Wyborn L, Hazell M, Page R, Idnurm M, Sun S (1998) A newly discovered major Proterozoic granite alteration system in the Mount Webb region, central Australia, and implications for Cu-Au mineralization. Aust Geol Surv Org 28:1–6

Young DN, Fanning CM, Shaw RD, Edgoose CJ, Blake DH, Page RW, Camacho A (1995) U-Pb zircon dating of tectonomagmatic events in the northern Arunta Inlier, central Australia. Precambrian Res 71: 45–68

Zhao JX, Bennett VC (1995) SHRIMP U–Pb zircon geochronology of granites in the Arunta Inlier, central Australia: implications for Proterozoic crustal evolution. Precambrian Res 71:17–43